Regional depth-specific subchondral bone density measures in osteoarthritic and normal distal femora: in vivo precision and preliminary comparisons

A Thesis Submitted to the College of

Graduate Studies and Research

In Partial Fulfillment of the Requirements

For the Degree of Master of Science

In the Department of Mechanical Engineering

University of Saskatchewan

Saskatoon

By

Alex Sacher

PERMISSION TO USE

In presenting this thesis/dissertation in partial fulfillment of the requirements for a Postgraduate degree from the University of Saskatchewan, I agree that the Libraries of this University may make it freely available for inspection. I further agree that permission for copying of this thesis/dissertation in any manner, in whole or in part, for scholarly purposes may be granted by the professor or professors who supervised my thesis/dissertation work or, in their absence, by the Head of the Department or the Dean of the College in which my thesis work was done. It is understood that any copying or publication or use of this thesis/dissertation or parts thereof for financial gain shall not be allowed without my written permission. It is also understood that due recognition shall be given to me and to the University of Saskatchewan in any scholarly use which may be made of any material in my thesis/dissertation.

DISCLAIMER

Reference in this thesis/dissertation to any specific commercial products, process, or service by trade name, trademark, manufacturer, or otherwise, does not constitute or imply its endorsement, recommendation, or favoring by the University of Saskatchewan. The views and opinions of the author expressed herein do not state or reflect those of the University of Saskatchewan, and shall not be used for advertising or product endorsement purposes. Requests for permission to copy or to make other uses of materials in this thesis/dissertation in whole or part should be addressed to:

Head of the Department of Mechanical Engineering

57 Campus Drive

University of Saskatchewan

Saskatoon, Saskatchewan S7N 5A9

Canada

OR

Dean

College of Graduate and Postdoctoral Studies

University of Saskatchewan

116 Thorvaldson Building, 110 Science Place

Saskatoon, Saskatchewan S7N 5C9

Canada

ABSTRACT

Knee osteoarthritis (OA) is a degenerative disease which affects the cartilage and underlying bone of afflicted joints. OA can be diagnosed by clinical symptoms such as joint pain, stiffness and swelling or radiographically according to the presence of key structural changes associated with the disease. The investigation of subchondral bone is a growing topic of interest in the study of OA, though its exact relationship with disease initiation and progression is currently not well understood. Previous studies have investigated subchondral bone's role in OA at the proximal tibia and patella; however there is a paucity of research at the distal femur. Additionally, many of the existing strategies to study subchondral bone in OA have relied on time-consuming manual techniques, limiting their applicability in studies with large sample sizes. This highlights a need for the development of automated techniques which assess subchondral bone at the distal femur.

The primary goal of this research was to develop an automated workflow capable of precisely assessing regional density measures at the distal femur to differentiate between OA and normal subjects. This resulted in the following objectives: 1) Develop an automated workflow for assessing regional density measures at the distal femur; 2) determine precision errors of the acquired density measures; and 3) compare distal femoral density measures between individuals with and without knee OA.

Following the development of an automated workflow, *in vivo* precision (assessed via root mean square coefficients of variation, $CV\%_{RMS}$) at the distal femur was assessed and ranged from 1.6% to 3.6%. These results are consistent with the *in vivo* precision errors found at the proximal tibia and patella, indicating they are suitable for investigating differences between OA and normal distal femora.

For the comparison analysis, mean regional density measures were not found to differ significantly between normal and OA distal femora; however, peak density clusters at depths of 2.5-5mm were found to be ~16% lower in OA distal femora.

Thesis results indicate that suitable precision can be obtained at the distal femur with automated methods. Results also suggest that subchondral density patterns may differ in OA and normal distal femora in complex ways, not necessarily detectable via regional analyses alone.

PREFACE

This research was performed by me with the exception of: CT imaging, which was completed by trained technicians, clinical OA diagnoses, which were conducted by a participating orthopedic surgeon, segmentation generation, which was generated by WD Burnett and research conception, which was developed by JD Johnston. Methodology development, data analysis and manuscript preparation were carried out by me with guidance from JD Johnston and SA Kontulainen.

Presentations:

A Sacher, W Burnett, D Wilson, J Hunter, S Kontulainen, J Johnston (2020). *Regional depth-specific subchondral bone density measures in osteoarthritic and normal distal femora: in vivo precision and links with pain*. 2020 Alberta Biomedical Engineering Conference

ACKNOWLEDGEMENTS

I would like to acknowledge all the people in my life that helped me throughout this process and made this work possible. First and foremost, I'd like to thank my supervisor Professor Johnston for his guidance and tenacity for the entirety of this project. Your ability to wade through discussions where we seemed to be speaking different languages highlight your patience and ultimately led us to many fruitful talks where we were on the same page.

I would also like to thank my mother, Colette, for the endless talks and words of encouragement. The many months of lockdowns and social distancing would likely have led to my insanity if it weren't for our many discussions and reassurances that I hadn't completely lost it. Your unwavering belief in me has been my primary source of motivation and has pushed me through some of the hardest times.

Equally as important but seldom praised, my father, Tony, should receive a proper acknowledgment. I owe a tremendous amount to the mountain of work you've done to allow me the time and energy to focus on my goals. Without your help, I envision myself becoming buried in life's challenges, unable to reach the same heights I am afforded with your support.

My fellow graduate students also deserve recognition for their contributions to this work. Thank you to Pablo, Tiffany, and Nassim for their assistance throughout our shared time together. Successfully navigating graduate school during the COVID lockdowns was only possible with your help. A special nod goes out to Pablo for being an excellent source of accountability during the transition to on-campus studies. Many unproductive 'work-from-home' days were avoided knowing you were on campus grinding away, compelling me to do the same.

Lastly, I want to thank Prof. Emily McWalter and Rob Peace for their words of wisdom throughout our many discussions. It is often difficult to obtain perspective on one's situation without the help of an outside voice to present things in a different manner. Rob and Emily provided that throughout my M.Sc., and served as excellent role models to remind me that hard work has intrinsic value, and will always pay off in one form or another.

TABLE OF CONTENTS

PERMISSION TO USE i

DISCLAIMER ii

ABSTRACT iii

ACKNOWLEDGEMENTS v

TABLE OF CONTENTS vi

TABLE OF FIGURES ix

TABLE OF TABLES x

LIST OF ABBREVIATIONS xi

GLOSSARY xiii

CHAPTER 1 OVERVIEW 1

1.1 Introduction 1

1.2 Scope 3

CHAPTER 2 LITERATURE REVIEW 4

2.1 Knee Joint Anatomy 4

2.2 Subchondral Bone 6

2.3 Radiographic OA signs 7

2.4 Imaging Modalities 8

2.5 Regional BMD Assessment 9

2.6 Cluster Analyses 10

2.7 Femoral Coordinate Systems 11

2.8 Alignment Techniques 12

2.9 Subchondral Surface Definition 14

CHAPTER 3 RESEARCH QUESTIONS AND OBJECTIVES 15

3.1 Research Questions 15
3.2 Research Objectives 15
CHAPTER 4 METHODOLOGY 16
4.1. Study Participants 16
4.2 OA Assessment 16
4.3 QCT Acquisition 17
4.4 Image Segmentation 17
4.5 Alignment Methodology 18
4.6 Subchondral Surface Definition 20
4.6.1 Template-based Definition 20
4.6.2 Subchondral Surface Refinement 22
4.7 Depth Definition 25
4.8 ROI Definition 26
4.9 Peak Density Clusters 27
4.10 Statistical Analysis 28
CHAPTER 5 RESULTS 30
5.1 Precision 30
5.2 Mean Regional BMD measurements 35
5.3 Peak Density Clusters 36
5.4 Post-hoc Power Analysis 41
CHAPTER 6 DISCUSSION 42
6.1 Overview of Findings 42
6.2 Study Strengths 45
6.3 Study Limitations 45

CHAPTER 7 CONCLUSION AND FUTURE WORK 47
7.1 Conclusions 47
7.2 Contributions 48
7.3 Future Research 48
LIST OF REFERENCES 50
APPENDIX A INITIAL ALIGNMENT AND K-MEANS METHODOLOGY DETAILS 56
APPENDIX B ALIGNMENT DETAILS 58
APPENDIX C SUBCHONDRAL SURFACE TEMPLATE-BASED DETAILS 61
APPENDIX D SUBCHONDRAL SURFACE REFINEMENT DETAILS 64
APPENDIX E ROI DEFINITION AND METHODOLOGY DETAILS 67

TABLE OF FIGURES

Figure 2-1 Knee joint anatomy 4

Figure 2-2 Articular Cartilage at the knee joint 4

Figure 2-3 Distal femur model 5

Figure 2-4 Illustration of varying contact surface of the distal femur in flexion and extension.... 6

Figure 2-5 Articular cartilage, subchondral cortical, and subchondral trabecular bone 6

Figure 2-6 Radiographs of healthy vs OA knee joint 7

Figure 2-7 Commonly used distal femoral axes 11

Figure 4-1 Sample transverse QCT slice with QCT reference phantom 18

Figure 4-2 Sample transverse QCT slice with segmented femur 18

Figure 4-3 Images of a sample output of the k-means algorithm 19

Figure 4-4 Distal femur transverse slice illustrating the PCL plane definition and alignment.... 19

Figure 4-5 Femoral anatomical axis definition and alignment 20

Figure 4-6 Process for defining subchondral start and end angles. 21

Figure 4-7 Template-based subchondral surface definition process 22

Figure 4-8 Sample 2D angular BMD map in grayscale colormap 23

Figure 4-9 Sample 2D angular distance map in grayscale colormap 23

Figure 4-10 Contrasted 2D angular distance map in colormap jet 24

Figure 4-11 Outline of refined subchondral surface 25

Figure 4-12 Refined subchondral surface volumes 25

Figure 4-13 Pelletier ROI diagram 26

Figure 4-14 MOAKS ROI diagram 27

Figure 4-15 Modified intercondylar fossa MOAKS region 27

Figure 5-1 Representative topographical color maps of average distal femoral BMD 36

TABLE OF TABLES

Table 4-1 Modified Kellgren-Lawrence (KL) Classification 16

Table 5-1 Precision results for mean regional BMD using the Pelletier ROI..... 31

Table 5-2 Precision results for mean regional BMD using the MOAKS ROI..... 32

Table 5-3 Precision results for PDC analysis at 0-2.5mm using the Pelletier ROI..... 33

Table 5-4 Precision results for PDC analysis at 0-2.5mm using the MOAKS ROI 33

Table 5-5 Precision results for PDC analysis at 2.5-5mm using the Pelletier ROI..... 34

Table 5-6 Precision results for PDC analysis at 2.5-5mm using the MOAKS ROI 34

Table 5-7 Mean BMD comparisons between OA and normal using the Pelletier ROI. 37

Table 5-8 Mean BMD comparisons between OA and normal using the MOAKS ROI. 38

Table 5-9 PDC comparisons between OA and normal at 0-2.5mm using the Pelletier ROI. 39

Table 5-10 PDC comparisons between OA and normal at 0-2.5mm using the MOAKS ROI. ... 39

Table 5-11 PDC comparisons between OA and normal at 2.5-5mm using the Pelletier ROI 40

Table 5-12 PDC comparisons between OA and normal at 2.5-5mm using the MOAKS ROI. ... 40

Table 6-1 Precision error comparison between distal femur, proximal tibia and patella..... 42

Table 6-2 Precision error comparison between unmodified and modified IF regions..... 43

LIST OF ABBREVIATIONS

Abbreviation	Description
2D	Two-dimensional
3D	Three-dimensional
BMD	Bone mineral density
BMI	Body mass index
CT	Computed Tomography
CV%	Percentage coefficient of variation
DOF	Degrees of freedom
DXA	Dual-energy x-ray absorptiometry
FEM	Finite element modeling
FDR	False discovery rate
HU	Houndsfield unit
IF	Intercondylar fossa
K_2HPO_4	Dipotassium phosphate
KL	Kellgren-Lawrence
MOAKS	MRI osteoarthritis knee score
MRI	Magnetic resonance imaging
OA	Osteoarthritis
PCL	Posterior condylar line
PDC	Peak density cluster
QCT	Quantitative computer tomography
RMS	Root mean square
ROI	Region of interest
SD	Standard deviation

TAP	Trochlear anteroposterior
TEA	Transepicondylar axis
WOMAC	Western Ontario and McMaster universities osteoarthritis index
WORMS	Whole-organ magnetic resonance imaging score

GLOSSARY

Term	Definition
Anterior	Anatomical direction indicating towards the front
Arthrography	Medical imaging after injection of a contrast medium to highlight tissues of interest
Automated	Operation or process performed without direct human control
Bone mineral density	General term relating to mass of bone per specified volume
Coronal	Anatomical plane which divides the body into anterior and posterior sections (front and back)
Cortical bone	Dense bone of the cortex; constitutes the outer shell of bones
Distal	Anatomical direction indicating away from the center of a body
Inferior	Anatomical direction indicating away from the head
In vivo	Latin for 'within the living'; pertains to research using an entire living organism
Joint space narrowing	Reduction in spacing between joints; associated with joint degeneration
Lateral	Anatomical direction indicating towards the sides
Medial	Anatomical direction indicating towards the middle
Osteophyte	Protrusion of bone emanating from the periphery of joint surfaces
Patellofemoral	Relating to anatomy involving the junction of the patella and distal femur
Pixel	Discrete element of an image in a gridded two-dimensional space
Posterior	Anatomical direction indicating towards the back
Proximal	Anatomical direction indicating towards the center of a body
Radiograph	Medical image produced using ionizing radiation; can be projectional (x-ray) or three-dimensional (CT)

Sagittal	Anatomical plane which divides the body into left and right sections
Sclerosis	State of locally increased bone density
Subchondral bone	Bone adjacent to cartilage and most involved with typical joint loading
Superior	Anatomical direction indicating towards the head
Tibiofemoral	Relating to anatomy involving the junction of the proximal tibia and distal femur
Trabecular bone	Porous bone typically found at the ends of long bones. Also known as cancellous or spongy bone
Transverse	Anatomical plane which divides the body into superior and inferior sections (top and bottom)
Voxel	Discrete element of a volume in a gridded three-dimensional space

CHAPTER 1
OVERVIEW

1.1 Introduction

Knee osteoarthritis (OA) is a complex degenerative joint disease marked by pain and altered cartilage and subchondral bone [1]. There are many known risk factors for OA, some of which are systemic (ethnicity, genetics, age) while others are biomechanical in nature (obesity, joint injury) [2]. Age in particular is a strong risk factor as approximately 14% of Canadians over the age of 20 suffer from OA, compared to 41% over the age of 75 [3]. The high prevalence of the disease resulted in a productivity cost of work loss of $12B in 2010 and is projected to grow to $17.5B by 2031 in Canada alone [4]. Another factor which contributes to OA's cost lies in the difficulty in early diagnosis. Many individuals do not have pain or dysfunction until they have developed significant tissue damage [5], suggesting that structural joint changes may precede clinical symptom expression. Those with OA can be diagnosed by their joint dysfunction, radiographic signs, or both. The relationship between radiographic evidence and clinical symptoms is not well understood [2].

Common clinical OA symptoms include joint pain, stiffness and swelling as well as loss of function [6]. The Western Ontario and McMaster Universities Osteoarthritis Index (WOMAC) [7] is a scoring system used to assess these symptoms, though it does not account for any radiographic signs. To quantify and assess radiographic anomalies, the Kellgren-Lawrence (KL) grading system [8] is most commonly used. Though both of these systems are widely accepted and employed, they are not sufficient to fully explain OA progression and status as one study found that only 47% of individuals exhibiting evidence of radiographic OA experienced associated clinical symptoms (e.g., pain) [9]. This discordance highlights the complex nature of the disease and suggests that more nuanced radiographic signs may be required to better explain OA status.

Aside from the large-scale anomalies which can be assessed using KL grading, researchers are investigating more subtle morphological and structural changes associated with OA initiation and progression. Notably, the exact role of subchondral bone in OA, as well as OA-related pain, is not well understood [10]. Subchondral bone is growing topic of interest in

OA research [11] as it is the bone directly adjacent to the cartilage, and is thought to be intimately linked with observed cartilage deterioration, a hallmark of OA [12]. It has been proposed that changes in subchondral bone structure or mechanical properties, such as stiffness, may precede cartilage damage and may play a significant role in OA initiation [12].

By viewing OA from a mechanical perspective, it is reasonable to conclude that subchondral bone has a key role in the disease. Whether changes in subchondral bone initiate OA or are a secondary feature, its altered mechanical properties directly affect the structural behavior of the joint and dictate how force flows through joint tissues [13] (i.e., a stiffer region of subchondral bone will support more load than a less stiff region). One such property, bone mineral density (BMD), is directly correlated to bone's elastic modulus [14] and can be used as a proxy for its relative strength [15]. BMD can also be readily assessed via several imaging modalities and has been widely used in the OA literature. By quantifying subchondral BMD, we can obtain a better understanding of its exact role within OA. Further, as previous work has shown that specific regions of subchondral bone may be affected more than others [16, 17], quantifying regional BMD may help to improve our understanding of OA pain pathogenesis, which is important for diagnostics and developing preventive and therapeutic treatments [18]. To date, research of this kind at the University of Saskatchewan has focused on the proximal tibia and patella. Our research group has not performed similar investigations at the distal femur.

The current evidence suggests that if links between distinct radiographic signs and clinical symptom expression exist, they are difficult to detect. Prior research [2, 16, 17] has controlled for obvious covariates, such as sex and BMI, but there are several others which are exceedingly difficult to account for (e.g., factors such as anatomical variations which affect joint loading patterns, cyst formation, and local cartilage degeneration will influence density patterns and may not be consistent across all individuals suffering with OA). To overcome this limitation, studies with high power (i.e., large sample sizes) are required to expose differences which may be obfuscated by the numerous confounding variables. Unfortunately, many of the existing strategies to study subchondral BMD in OA have required significant human involvement. Consequently, much of this involvement is expensive and time-intensive, creating challenges in applying these methods to datasets with large sample sizes (e.g., 2000+ participants). This highlights the importance of developing automated workflows which can assess subchondral

BMD, improving the feasibility of conducting such analyses at larger scales.

1.2 Scope

Chapter 2 provides a literature review of the relevant background information, previous research and knee joint anatomy. Chapter 3 outlines the proposed research questions and objectives. Chapter 4 describes the methodology for accomplishing all stages of this research. Chapters 5 and 6 contain a report and discussion of this work's results, including study strengths and limitations. Lastly, Chapter 7 provides the conclusions, contributions and directions for future work related to this research.

CHAPTER 2
LITERATURE REVIEW

2.1 Knee Joint Anatomy

OA can present in many joints of the body, with the knee being one of the most commonly afflicted sites [19] and the focus of this work. The knee joint is a synovial joint which is comprised of four bones: femur, tibia, fibula, and patella. A synovial joint is characterized as having an enclosed capsule filled with synovial fluid which surrounds the articulating surface. Tendons connect the many muscles of the joint with the bones, while ligaments connect between bones. These tissues provide the joint with sufficient stability and strength and alongside the nearby muscles, allows for several forms of motion at the knee. Two menisci are situated medially and laterally between the tibia and femur, which help to distribute load between the bones and add stability to the joint. Cartilage, a thin, elastic tissue is found on all articulating surfaces of the bones and helps to reduce friction, allowing for smooth movement. Figure 2-1 shows a posterior view of the knee joint and associated anatomy. Figure 2-2 shows the location of articular cartilage at the tibia and femur.

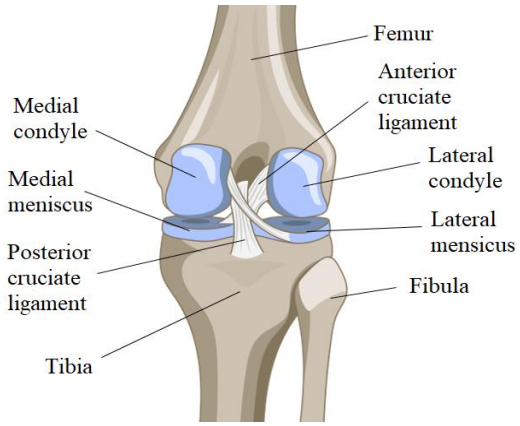

Figure 2-1 Knee joint anatomy (from DataBase Center for Life Sciences, accessed via Wikimedia Commons under Creative Commons Attribution 4.0)

Figure 2-2 Articular Cartilage at the knee joint (from user crevis accessed via Adobe Stock under standard licensing)

In this document, the three principal anatomical planes (sagittal, coronal and transverse) are used to spatially define key points and orient the reader. Anatomical directions are similarly used for this end. Figure 2-3 shows the distal femur from directions normal to each anatomical plane, accompanied by local anatomical directions.

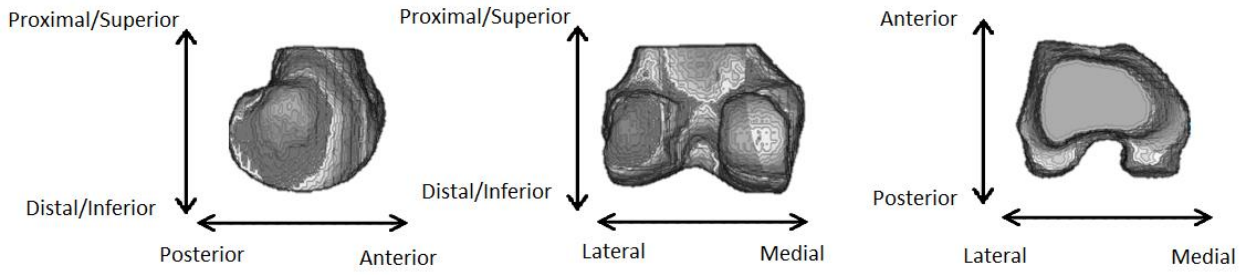

Figure 2-3 Distal femur model viewed from normal to sagittal (left), coronal (middle), and transverse (right) planes

The local anatomy of the distal femur has some noteworthy features in the context of this work. The femoral condyles are bony features found on both medial and lateral sides of the distal femur. More anterior and superior are pronounced edges of the femur called epicondyles. Both features have been used as landmarks in femoral coordinate systems [20-22] and are used in this work for similar ends. The intercondylar fossa (or intercondylar notch) is a concave feature situated posteriorly between the condyles. It is not involved with any joint contact, though is the site of several major stabilizing structures of the knee joint [23]. As a result, the bone in this area typically exhibits high densities compared to surrounding tissues.

The distal femur is directly involved with both the patellofemoral and tibiofemoral joints. This is noteworthy as the articulating surface of the distal femur is highly curved and has indistinct boundaries separating one joint contact surface from the other. In fact, joint contact surfaces will vary during knee flexion and extension. During knee flexion (i.e., bending knee), patellofemoral contact occurs more centrally, while tibiofemoral contract will occur more posteriorly. Alternatively, during knee extension (i.e., straightening knee), patellofemoral contact occurs anteriorly, while tibiofemoral contact occurs in the central portion of the distal femur. Figure 2-4 illustrates the different contact surfaces during both flexion and extension. These varying contact angles are important as they directly affect loading patterns and resulting density distributions throughout the distal femur.

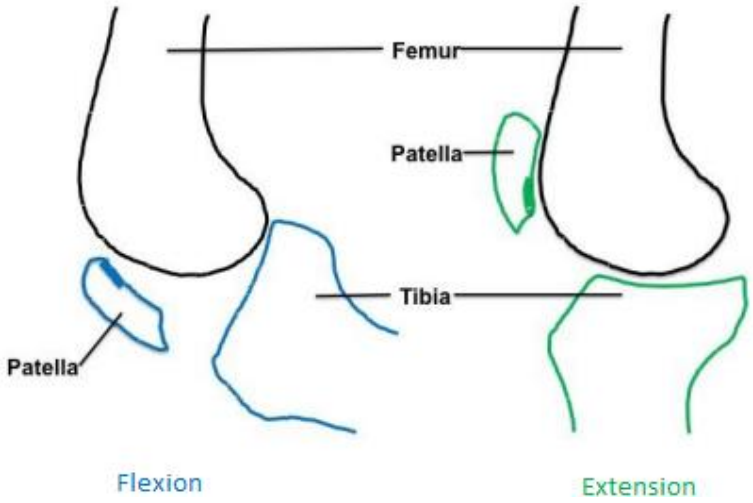

Figure 2-4 Illustration of varying contact surface of the distal femur in flexion and extension. Adapted from Burnett et al.

2.2 Subchondral Bone

The region of bone directly adjacent to articular cartilage is characterized as ‘subchondral’. Subchondral bone is comprised of both cortical and trabecular bone and is typically the joint’s main supportive structure [13]; acting in series with cartilage to transfer force through the joint. Figure 2-5 provides a schematic of various layers of the cartilage-subchondral bone complex.

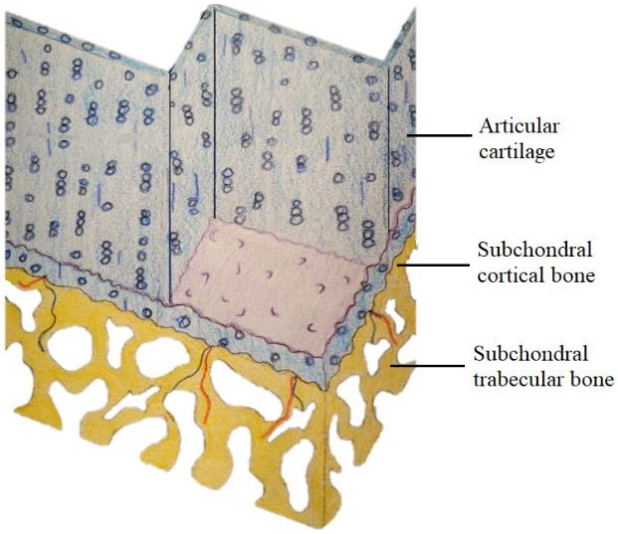

Figure 2-5 Schematic drawing displaying articular cartilage, subchondral cortical bone, and subchondral trabecular bone

Subchondral bone appears to play a significant role in OA development and pathogenesis, however, the specific mechanical alterations at various stages of the disease are not well understood. Alterations in trabecular bone mass and architecture as well as subchondral bone plate thickening are common in those with OA [24]. An ongoing debate questions if subchondral bone alterations initiate OA or if they are a consequence of it [12]: local inceptive changes in subchondral bone may initiate joint degeneration by disrupting the mechanical environment, damaging surrounding tissues. Conversely, adaptive remodeling of these tissues during disease initiation and progression is to be expected due to the significant mechanical role it plays. More research is needed to elucidate the relationship between subchondral bone alterations and OA.

2.3 Radiographic OA signs

OA often presents with visible alterations to many tissues of the afflicted joint. Progressive cartilage loss, synovial inflammation and meniscal damage are common soft-tissue signs associated with knee OA [1]. These changes can lead to joint space narrowing, another hallmark of OA. Bony features such as osteophytes and cysts as well as subchondral sclerosis (i.e., increased density) are also key alterations which characterize OA. Figure 2-5 shows a radiograph comparison of a visually healthy knee joint versus one displaying signs of OA.

Figure 2-6 Radiographs of healthy (left) vs OA (right) knee (from user Ptrump16 accessed via Wikimedia commons under Creative Commons Attribution 4.0 and from Richman Photo accessed via Adobe Stock with a standard license)

Subchondral BMD is a property which has been widely studied in OA, though multiple conflicting trends have been reported. Previous work has shown that individuals with OA have: higher BMD [25-27], lower BMD [27, 28], normal BMD [29, 30]. These findings, coupled with the high prevalence of asymptomatic radiographic OA [9], indicate more research is needed to elucidate the role of subchondral BMD in the disease. Further, accounting for regional BMD differences may provide additional insight as prior research [16, 17] has shown specific regions may be more closely linked with OA-related pain than others.

2.4 Imaging Modalities

Several imaging modalities have previously been used to assess and investigate OA, both in a clinical diagnostic and research context. However, to properly assess regional BMD, careful consideration must be given to the chosen imaging modality. For clinical applications, radiographs are commonly used as they are inexpensive, readily available and can display the features used in KL grading. However, x-ray radiographs are two-dimensional and do not provide any quantitative data relating to tissue properties (e.g., regional BMD), limiting the analyses which can be performed.

Dual-energy x-ray absorptiometry (DXA) overcomes the quantitative limitation of radiographs and is commonly used to assess areal bone mineral density (aBMD) for osteoarthritis research and diagnosis [25-27]. However, the two-dimensional projection nature of DXA is subject to errors caused from patient size and positioning differences [31] and is therefore difficult to perform regional assessments with.

To allow for the true regional assessment of joint tissues, 3D imaging modalities must be used. Magnetic resonance imaging (MRI), which has excellent soft tissue contrast, has been used for this end in both diagnostic and research contexts via the Whole-Organ Magnetic Resonance Imaging Score (WORMS) [32]. MRI has also been used to assess quantitative differences found in the tissues of afflicted OA joints [33]. However, it can be challenging to characterize bone using MRI because it is primarily composed of calcium hydroxyapatite, which has only one proton which does not move. The decay time of bone is therefore very short and minimal signal arises [34]. This leads to the bone appearing mostly black in the image, making it difficult to quantify BMD from MRI alone [35].

Quantitative Computed Tomography (QCT) is an imaging modality which can derive 3D images of structures and assess localized BMD at individual voxels. This is done via calibration phantoms which convert the native Hounsfield Units (HU) to equivalent volumetric BMD. This allows for independent regional analysis and overcomes many of the limitations of the previously described imaging modalities for regional BMD assessment. As a result, QCT has been widely used to investigate BMD in the context of OA research and is a suitable imaging modality for assessing regional subchondral BMD at the distal femur.

2.5 Regional BMD Assessment

Previous work by Burnett et al. found relationships between regional subchondral BMD and OA-related pain at the tibia [16, 36] and patella [17]; though currently, no studies have investigated similar trends at the distal femur. Acquiring regional BMD data at the distal femur is needed to provide a complete picture of the subchondral bone density profiles associated with OA at the knee. The previous research in this area provides suitable templates to build from; though, differences in the bone of interest and desired application will require modification to the previous methodologies. Most notably, novel approaches will be required for defining depth and sub-regions to account for the highly curved contact surface of the distal femur.

Specifically, depth assessment for the highly curved distal femur will require an alternative to the previously applied density projection technique used at the proximal tibia and patella, which is meant for relatively flat structures. Additionally, careful attention must be given to the relevant depth of the subchondral bone which is to be analyzed. Omoumi et al. chose to analyze to a depth of 3mm [37], while Johnston et al. and Burnett et al. chose to assess varying levels of depth ranging from 0 to 10mm [16, 38, 39], with the first 2.5mm assumed to be cortical bone. The rationale behind these choices likely stems from work done in [40] showing much of the high strength bone is present within the first 5mm of the bone's surface, suggesting this bone plays the largest mechanical role and therefore should be the site of adaptive or degenerative changes due to OA.

The division of the distal femoral subchondral region into relevant sub-regions is also an important design choice. Omoumi et al. found that OA affected relationships between medial and lateral sub-regions in both the proximal tibia and distal femur [37], though their regions of

interest (ROI) were limited to only a portion of the load-bearing surface. Further research that elucidates which regions are most affected by OA may provide additional insight into the nature of the disease. Favre et al. provide an overview of several femoral cartilage sub-regions of interest which have previously been used in the literature [41]. These cartilage ROIs could be mirrored to the distal femur and used for regional BMD assessments. Similarly, Hunter et al. identified limitations in the existing WORMS scoring methods and developed the MRI Osteoarthritis Knee Score (MOAKS) [37]. The MOAKS approach is an extension of the WORMS method, but includes the additional evaluation of distinct predefined sub-regions. The distal femur is divided into 6 regions (lateral/medial and anterior/central/posterior). This method could also be applied to define sub-regions of the subchondral surface for BMD assessment, making it well-suited for studying links with overlying cartilage degeneration

Lastly, most studies to date have used workflows which require significant human involvement to manually define regions of interest or important landmarks. This involvement is usually time intensive thereby making such methods infeasible to apply to large datasets such as the Multicenter Osteoarthritis Study (MOST), a study of +2000 individuals across the United States with different levels of knee OA progression and pain [42]. This is noteworthy as there are an abundance of confounding variables that may affect underlying subchondral BMD patterns which cannot be easily accounted for. It is possible that this limitation could be overcome by conducting automated subchondral BMD assessments on a larger scale, thereby minimizing the effects of uncontrolled variables.

2.6 Cluster Analyses

In addition to mean regional BMD measures, there is growing interest in cluster analyses. Here, instead of assessing average BMD of entire regions, these analyses focus on characterizing a collection or ‘cluster’ of connected voxels which meet certain thresholds. Previous studies have used clusters for failure criteria [43] and to identify focal cartilage lesions [44]. From a mechanical perspective, it is reasonable to hypothesize that lesions present in femoral cartilage would lead to a corresponding region of altered density subchondral bone due to a local change in stress. It therefore may be useful to characterize local clusters of high-density subchondral bone as a possible marker of OA-related joint degeneration. This approach could succeed in identifying abnormal density patterns where regional measures fail, as bone alterations

associated with OA may lead to low-density bone surrounding the high-density clusters (or vice-versa), resulting in unexceptional mean regional BMD measures.

2.7 Femoral Coordinate Systems

When investigating anatomical features, considerable attention must be given to the positioning of the tissues of interest. Typically, small variations in patient positioning and anatomy lead to captured images which do not have consistent orientations. In order to make subject-to-subject comparisons, as well as conduct longitudinal analyses, each imaged tissue of interest must therefore be realigned in a standard, repeatable position. Further, orientations which are established in the literature and widely known amongst clinicians should be used to facilitate comparisons between studies. This step is particularly important for regional analyses as each individual region must be consistently defined for each image.

Several femoral coordinate systems and axes have been used in the literature with varying frequency. Victor provides insight into some of these axes in their 2009 literature review [45]. The posterior condylar line (PCL), transepicondylar axis (TEA), trochlear anteroposterior (TAP) axis, and femoral transverse axis have all been used in literature with varying popularity. An image of these axes can be seen in Figure 2-6.

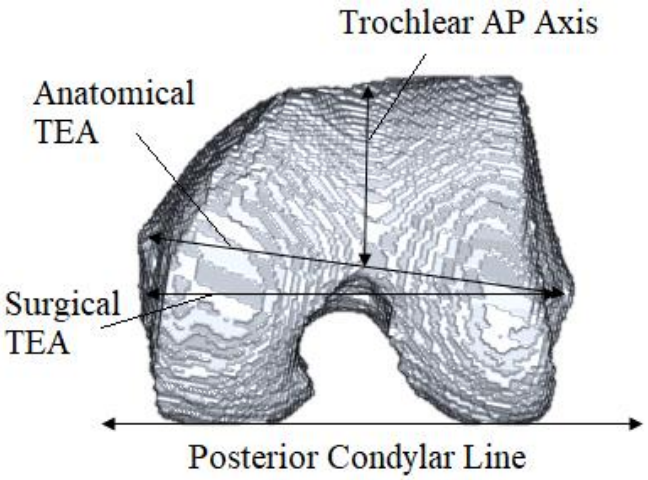

Figure 2-7 Commonly used distal femoral axes in surgical research and application

It is important to note that this review was created in a clinical surgical context, while for our purposes, it must be considered in conjunction with the OA literature. The femoral mechanical

axis was not included in the review, though it has been used for alignment purposes in the OA [46] and computer model [21] literature. The PCL is a common reference axis in many studies investigating OA as it is unambiguous and easily located [46, 47]. To fully orient a femur object in 3-dimensional Euclidean space, relationships must be defined for all 3 axes. Some studies have approached this issue by assuming fixed coronal and/or sagittal plane rotations [47]. This may be reasonable for small studies with very consistent patient positioning; however, in applications where data originates from many different sources (such as large datasets), this assumption may not be appropriate.

Of note, there is a distinction which must be made on the topic of anatomical correspondence. Often, anatomical correspondence is achieved by defining an axis or set of axes and aligning the anatomy of interest from them. This leads to an 'overall' alignment where only these predefined axes are matched. However, due to inter-subject anatomical variability, alignment of specific axes may not lead to suitable correspondence of a pre-defined sub-region. This issue is relevant for this research as the alignment methodology should facilitate subchondral bone region comparisons. Therefore, careful consideration must be given to employ alignment methodologies which are conducive to achieving consistent correspondence of the subchondral surface.

2.8 Alignment Techniques

Previous techniques explored in the literature have relied on the manual selection of boundary points or physical landmarks to define standardized alignments and regions of interest [38, 46, 48-50]. Though these methods were effective for repeated alignment, human involvement was necessary to accurately select landmarks. Automating this task may be feasible, though landmark detection at the distal femur may be challenging due to the indistinct features and significant anatomical variability typically observed at this site.

A popular semi-automated approach to address this problem is to fit shapes of known geometry to the object using best-fit or dimensionality reduction techniques [38, 41, 47-50]. This can simplify the region of interest (ROI) geometry and provides an intuitive method for collecting standardized measurements. This method is especially useful when the ROI is completely contained within the fitted shape or is in close proximity. However, registering

simple shapes to complex geometries is limited to coarse alignments and may not provide sufficient accuracy to allow for consistent region definition. Specifically, defining femoral anatomical axes from such a registration would be challenging and may not yield accurate or repeatable results. Therefore, it is likely not suitable for the task of automated alignment.

A multi-step computational anatomy-based process was proposed by Babel et. al for proximal tibia registration [51]. The process begins with a rigid registration to match the general shape of a moving tibia to that of a fixed reference tibia. Subsequent rigid and non-rigid transformations are applied to the moving tibia to further match its surface to that of the reference tibia. The voxel values are modified according to the applied transformations to preserve image intensity information. In this approach, comparisons between subjects can be done at a voxel level, though large-scale geometry variations and differences in surface curvature and local geometry likely require significant distortions to BMD values. Significant local deformations may be required in some cases, potentially altering the original spatial distribution of BMD. This issue would likely be further complicated by the presence of osteophytes and subchondral cysts, common features associated with OA. Large scale transformations would result in the voxels of these bony features being averaged among those nearby, possibly misrepresenting BMD values.

The technique proposed by Babel et al., was also adapted for use at the distal femur [52], though significant modifications were required. First, the rigid registration to a fixed model was replaced with a cylindrical shape fitting step. Secondly, the trochlear notch was manually located and used to match the femur shapes. Scaling and rotations were then applied to match the cylinders of the moving and fixed femurs with a final step of local deformations to achieve close correspondence between the two objects. Again, this computational anatomy-based approach focused on achieving a coarse initial alignment then applying non-rigid transformations to achieve object conformity, sharing the strengths and limitations of the technique used at the tibia.

Fischer et al. [21] describe a novel workflow to automate the identification of femoral landmarks, planes and coordinate systems using surface models. This process has potential; though, currently it requires the full femur bone to be present, which is rare with QCT imaging data as the radiosensitive pelvic region is rarely scanned. The authors do reference [22] where

axes were determined from distal femora only. The process determines mediolateral axes by characterizing condyle shape alone. This process, and other similar geometry-based methods, could be adapted for this work.

2.9 Subchondral Surface Definition

Many previous studies using manual segmentation techniques have added an additional step of segmenting cartilage from each slice [37, 47, 51]. With the cartilage defined, the subchondral area can be easily determined for each bone. However, cartilage is not visible with QCT imaging (without the use of arthrography), and therefore it is not possible for investigations using only QCT to include this step. Therefore, when working from QCT images alone, the subchondral area must be defined without knowledge of the true cartilage location.

In [37], Omoumi et al. manually applied 3D maps based on the estimated anatomical location of cartilage in order to define a subchondral area on femur and tibia objects. Another method, which used projection mapping of the highest density voxels of the contact surface, was used in [39] to guide placement of boundary points. In the context of automating the process, both techniques have strengths and limitations. Specifically, using predefined maps is a simple to implement technique which will roughly match the expected shape of the subchondral bone but will apply the same map regardless of the individual geometries of each femur. This may result in poor performance on femora with irregular shape. Conversely, defining the subchondral bone in reference to locations of higher density may provide a more robust method to delineate the subchondral region regardless of femur geometry; however, this method may have an unintended outcome as it may ignore potential differences between healthy and OA femora (i.e., differences in BMD patterns between healthy and OA femora could influence the defined shape of the subchondral region using this method).

An approach which may be optimal for automating this process could include elements of both approaches and create a scheme in which high density voxels are used as a placement guide to apply a generic subchondral map. The map would have a consistent size (relative to the femur size) but could be locally stretched to ensure the high-density subchondral regions are contained within it. This could improve the consistency of the process as the subchondral bone would maintain an expected high-density profile, regardless of irregular femur geometry.

CHAPTER 3
RESEARCH QUESTIONS AND OBJECTIVES

3.1 Research Questions

Two questions which motivate this research are:

- Can distal femoral subchondral BMD be assessed precisely without manual intervention?
- Does distal femoral subchondral BMD differ between individuals with and without knee OA?

3.3 Hypothesis

From the 2nd research question, we can formulate an appropriate hypothesis for this work: distal femoral subchondral BMD differs between individuals with and without knee OA.

3.2 Research Objectives

To address these research questions and test the stated hypothesis, this work has three proposed objectives:

1. Develop an automated image processing algorithm for assessing regional and depth-specific BMD at the distal femur
2. Determine precision errors of the distal femoral regional density measures
3. Compare distal femoral regional density measures in individuals with and without knee OA

CHAPTER 4
METHODOLOGY

4.1. Study Participants

The New England Baptist Hospital dataset was used for this research. It is composed of fourteen participants (2 men and 12 women; mean age 51.4, SD 11.8 years) with repeat QCT scans of the knee. Informed consent was obtained for all participants and institutional review board approval was acquired prior to the study initiation.

4.2 OA Assessment

If the participant was experiencing knee pain, that knee was selected for imaging. Radiographic knee OA assessments were performed by a collaborating orthopedic surgeon using QCT imaging data with a modified Kellgren-Lawrence (mKL) OA severity scoring system (modified as in participants were laying down in the CT scanner, making joint space narrowing characterizations challenging). The OA severity classifications used in this study are given in Table 4-1.

Table 4-1 Modified Kellgren-Lawrence (mKL) Classification used in this research

Modified KL Grade	Visible OA Signs
0	Normal, no osteophytes
1	Possible osteophyte lipping
2	Definite osteophytes, possible joint space narrowing
3	Moderate or multiple osteophytes, definite joint space narrowing, some sclerosis and possible bony deformity
4	Large osteophytes, marked joint space narrowing, severe sclerosis, and definite bony deformity

Seven of the fourteen imaged knees displayed radiographic evidence of OA and were subsequently assigned to the OA group (1M, 6F; 52.4 ± 8.7 years; 1 with mKL = 1; 3 with mKL

= 2; 2 with mKL = 3; 1 with mKL = 4). Conversely, the remaining seven knees showed no radiographic evidence of OA and were assigned to the normal group (mKL = 0).

4.3 QCT Acquisition

Each participant's knee of interest was imaged with single-energy QCT acquired by a clinical CT scanner (Lightspeed 4-slice, General Electric, Milwaukee, WI, USA). Each participant was instructed to lay in the supine position with their knee centered within the CT gantry. A solid QCT reference phantom (Model 3T; Mindways Software Inc, Austin, TX, USA) was also placed within the gantry to allow for the conversion between the native Hounsfield units (HU) to an equivalent apparent volumetric BMD (mg/cm^3 K_2HPO_4). This was done via a linear regression equation ($R^2 > 0.99$) which was derived from the mean Hounsfield unit intensities and the known reference phantom densities. Selected scanning parameters used were: 120 kVp tube voltage, 150 mA tube current, axial scanning plane, 0.625 mm isotropic voxel size, ~240 slices, ~1.5 minute scan time. A standard bone kernel (BONE) was used for edge enhancement and post-processing. Participants were imaged in this manner three times over two days to produce three sets of QCT images (which is needed for characterizing measurement precision errors). Figure 4-1 shows a sample single QCT slice with the reference phantom in view.

4.4 Image Segmentation

In order to delineate bone from the surrounding soft tissue, each scan was segmented using a semi-automatic region growing technique via commercial software (Analyze10.0; Mayo Foundation, Rochester, MN, USA). A half maximum height technique was used to determine the subject-specific bone threshold for each image. This threshold is approximately equal to a voxel which contains 50% cortical bone and 50% joint space. This process was done for the distal femur, proximal tibia, and proximal fibula. Lastly, manual corrections were performed using a stylus and a touch-screen tablet (Cintiq 21uX, Wacom, Krefeld, Germany). Figure 4-2 shows a transverse slice of a segmented distal femur volume.

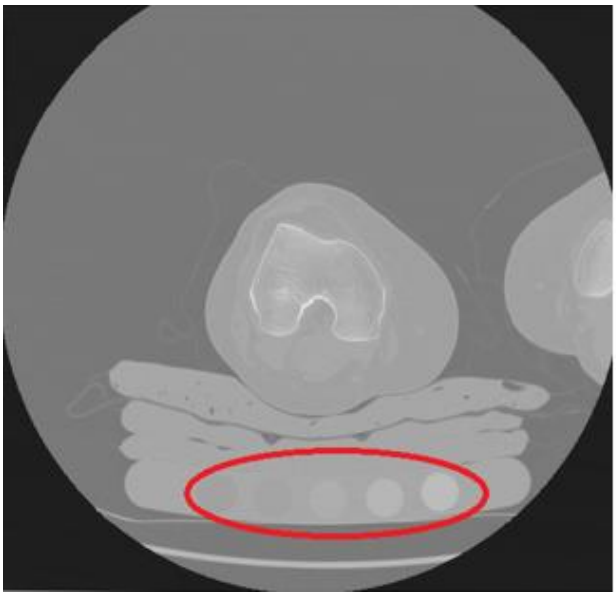

Figure 4-1 Sample transverse QCT slice with QCT reference phantom circled in red

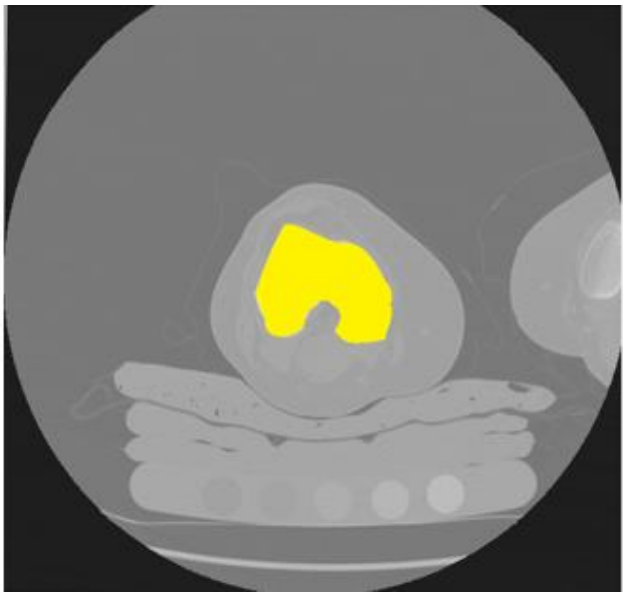

Figure 4-2 Sample transverse QCT slice with segmented femur volume shown in yellow

4.5 Alignment Methodology

A fully automated alignment protocol was developed to standardize the orientation of each segmented distal femur volume. Pre-alignment steps assess the initial positioning and orientation of each segmented femur to facilitate future alignment steps. This is done by applying the k-means clustering algorithm (with n = 2) to the segmented volume and assessing the resulting clusters. Due to the geometry of the distal femur, the clusters will consistently be assigned such that each condyle is classified separately from the other. Figure 4-3 provides a sample output of the k-means cluster. Thorough testing yielded that this process is insensitive to random initial cluster centers and will converge to the expected outcome. By assessing the geometry of each cluster, the general orientation can be deduced by the morphological differences between the lateral and medial condyles. Once the clusters have been classified as medial or lateral, further geometry-based techniques mirror right femora to be left, and orient the volume in a roughly neutral orientation. Additional details on these methods are provided in Appendix A.

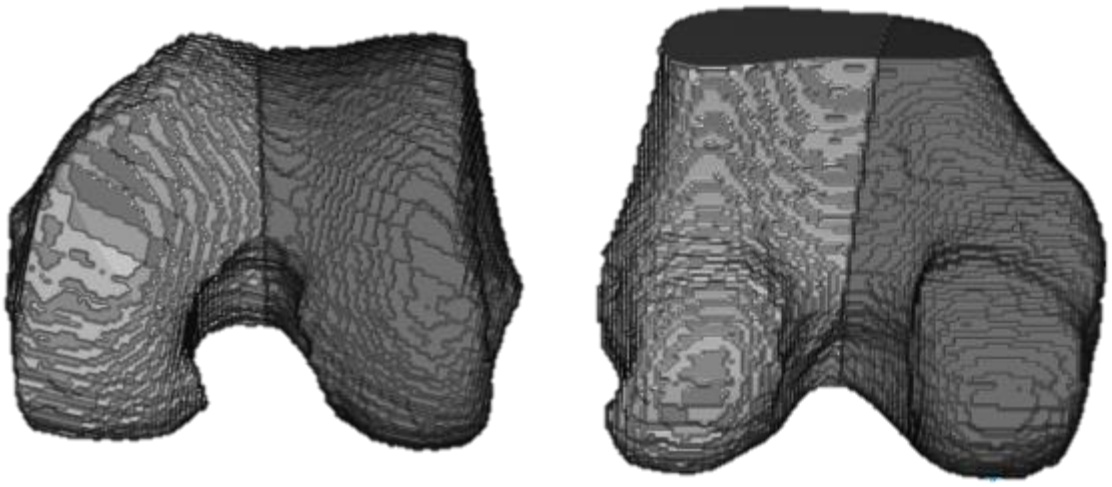

Figure 4-3 Images of a sample output of the k-means algorithm, dividing the distal femur volume into two medial/lateral halves

To refine on this orientation, axes are defined and used to align each femur in a standard coordinate system. First, the femur is rotated in the transverse plane so that the PCL is horizontal when viewed superiorly. The resulting normal from the PCL plane is considered the first axis (Figure 4-4). Next, a 2D 'shell' image is created by subtracting a sagittal projection of the femur by a sagittal slice located at the intercondylar fossa (Figure 4-5A). This resulting image consistently includes a gap along the direction of the femoral neck. The edges of this gap are then used to calculate a 2nd axis which approximates the femoral anatomical axis (Figure 4-5B). Further details on this process are provided in Appendix B.

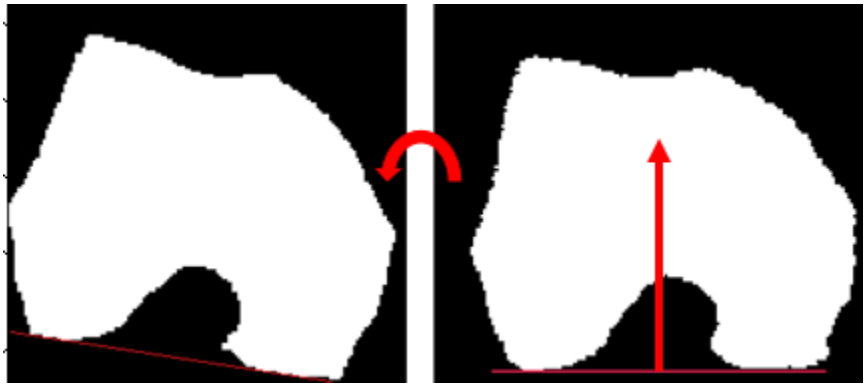

Figure 4-4 Transverse slice of the distal femur illustrating the PCL plane definition and alignment

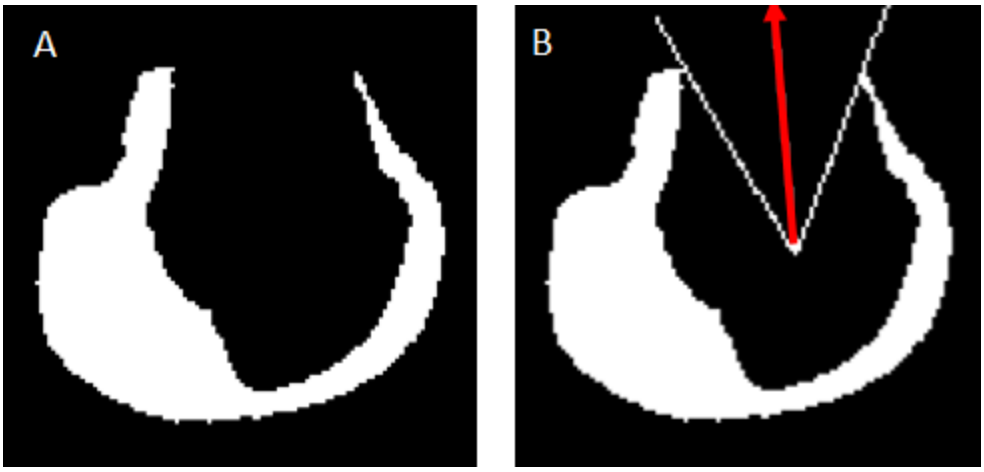

Figure 4-5 Femoral anatomical axis definition and alignment (A) 2D distal femur 'shell' image created from subtracting a sagittal slice at the intercondylar fossa (approximate sagittal center of the distal femur) from a sagittal slice containing the full breadth of a condyle (B) Resulting femoral anatomical axis calculated as the midpoint angle of the 'shell' image femoral neck opening

4.6 Subchondral Surface Definition

The subchondral surface was delineated from the surrounding bone in a general 2-step process:

1) Coarse, template based definition
2) Edge refinement via density and geometry based corrections

This two-step approach was implemented as anatomical variation presents a challenge in uniformly applying set rules to delineate the subchondral surface from the surrounding bone. The major advantage of using this approach is that spatial information obtained in the first step can be leveraged to guide the sensitive location of the subchondral surface borders, mitigating error.

4.6.1 Template-based Definition

The template-based definition process begins by estimating the most posterior and anterior aspects of the articulating surface. This is achieved by using the 2D 'shell' image described in Section 4.6 (Figure 4-5A). The thickness of the shell is computed for each angle with respect to the femoral centroid, resulting in a plot which characterizes its shape (Figure 4-6A). The rate of change of this plot is then calculated (Figure 4-6B), and the first large drop in thickness is identified from it. The angle of this large drop represents the approximate transition from the round condyle to the straighter posterior side of the femoral neck (Figure 4-6C). Though this

transition point may not consistently mark the end of the subchondral surface, it is a repeatable feature which can be used as an approximate start. The most anterior angle of the articulating surface is then found by reflecting the posterior angle with the previously determined transverse axis (Figure 4-6D).

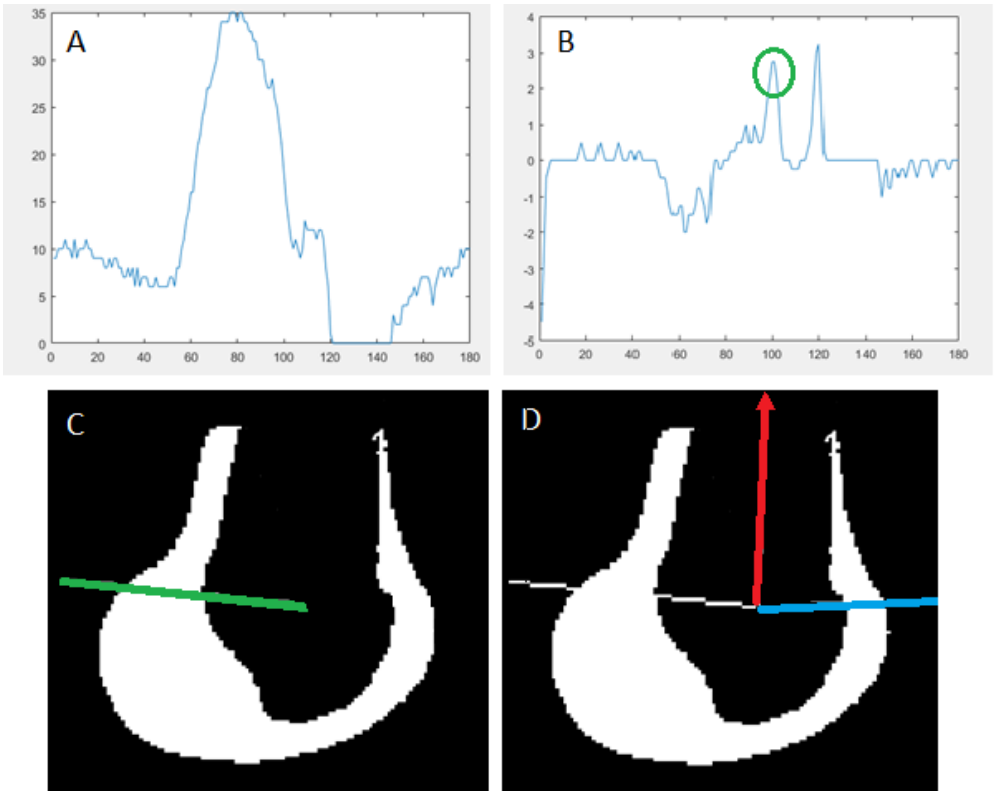

Figure 4-6 Process for defining subchondral start and end angles for the template-based approach (A) Sample plot showing femoral 'shell' thickness (y-axis) as a function of angular position with respect to the femoral centroid (x-axis) (B) Sample plot showing the negative rate of change of the plot in Figure 4-6A. The first peak (circled in green) corresponds to the (C) posterior angle marking the transition from condyle to femoral neck (D) Anterior angle (coloured in blue) found by reflecting the posterior angle by the anatomical femoral axis (coloured in red).

Next, femoral landmarks representing boundaries between pre-defined sagittal regions are located (Figure 4-7A) so that a generic cartilage-shaped template can be locally deformed to align with these regions (Figure 4-7B). Lastly, the adjusted cartilage map is overlaid with the femur volume such that the extreme ends of the map align with the previously estimated anterior and posterior end angles of the articulating surface (Figure 4-7C). This results in a distal femur object with a surface layer of delineated voxels (Figure 4-7D) and concludes the template-based definition step. Additional details of this process are outlined in Appendix C.

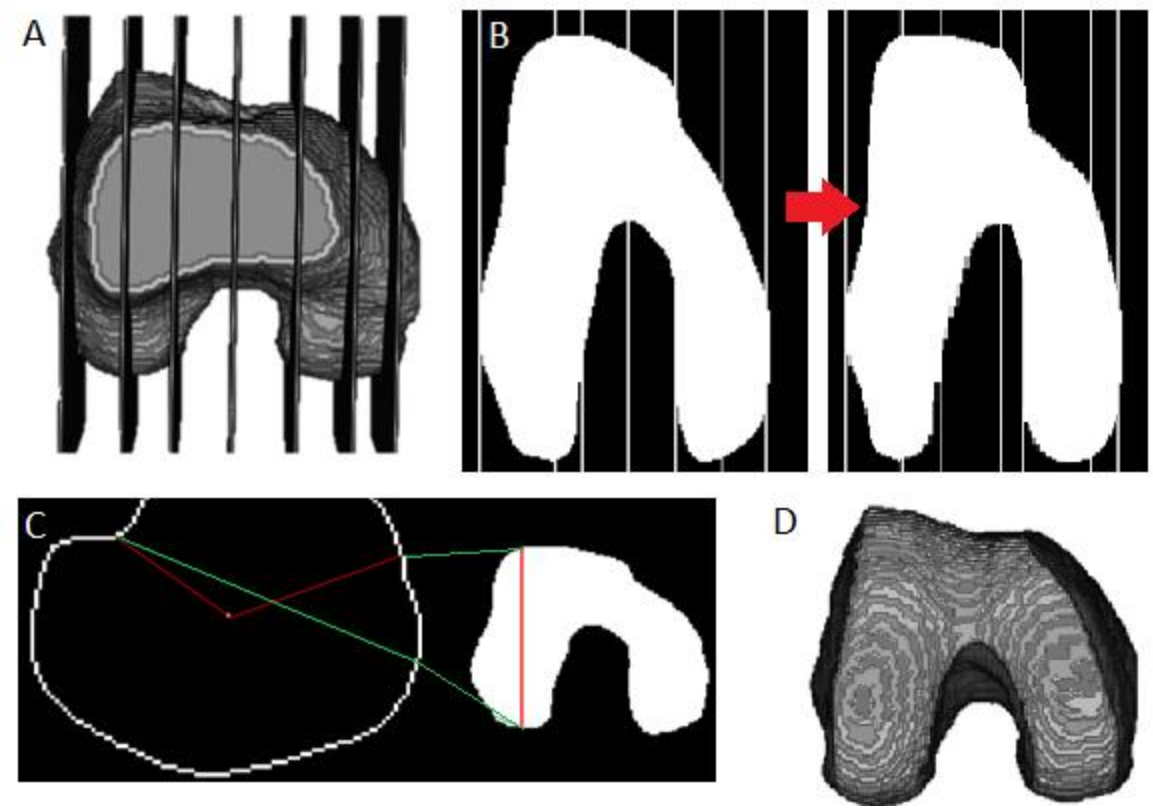

Figure 4-7 Template-based subchondral surface definition process (A) Sagittal plane landmarks are located on the distal femur via geometry-based techniques, splitting the volume into predefined regions. The subchondral template is locally deformed to match the dimensions of these regions (B). The template is then applied to the volume using the previously found posterior and anterior end angles (C), resulting in a delineated subchondral surface overlaid on the distal femur volume (D)

4.6.2 Subchondral Surface Refinement

A custom method to represent the femoral density information based on the 'binning' process in [44] was created and used to better define and delineate the subchondral surface from the surrounding bone. The sagittal and angular positions (with respect to the femur centroid) of each voxel are calculated and used as the input for a scatter interpolation. The interpolant can then be evaluated at regular intervals to create a 2D map which displays the distal femur with the x axis corresponding to the angle that voxel makes with the centroid. Figure 4-8 shows an example of the 2D angular BMD map.

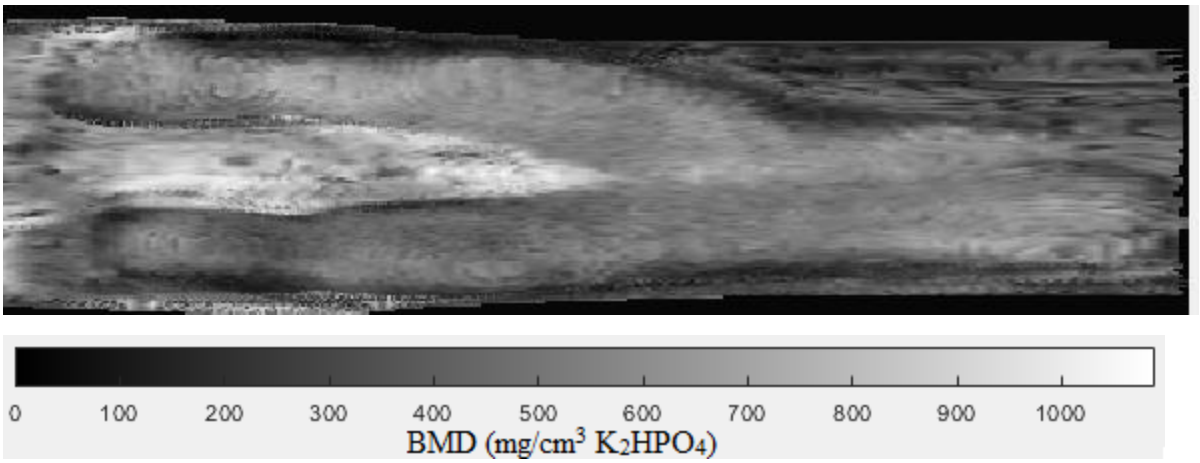

Figure 4-8 Sample image of a 2D angular BMD map in grayscale colormap

A rough outline of the subchondral surface can be visually identified by human observers in this view; however, the complete automatic segmentation of this region could not be achieved in this work. Therefore, only the most consistent characteristics of the 2D BMD maps were used to refine the subchondral surface. For example, regions of highly stochastic values tend to indicate an area with steep curvature such as the medial and lateral edges of condyles, information which can refine the borders of the subchondral region.

A secondary plot can be created by replacing the BMD values with the distance between each voxel and the centroid voxel. This plot reveals important geometry information, but since BMD is not included, it cannot distinguish high-density subchondral bone from surrounding bone. An example of a 2D angular distance map is shown in Figure 4-9.

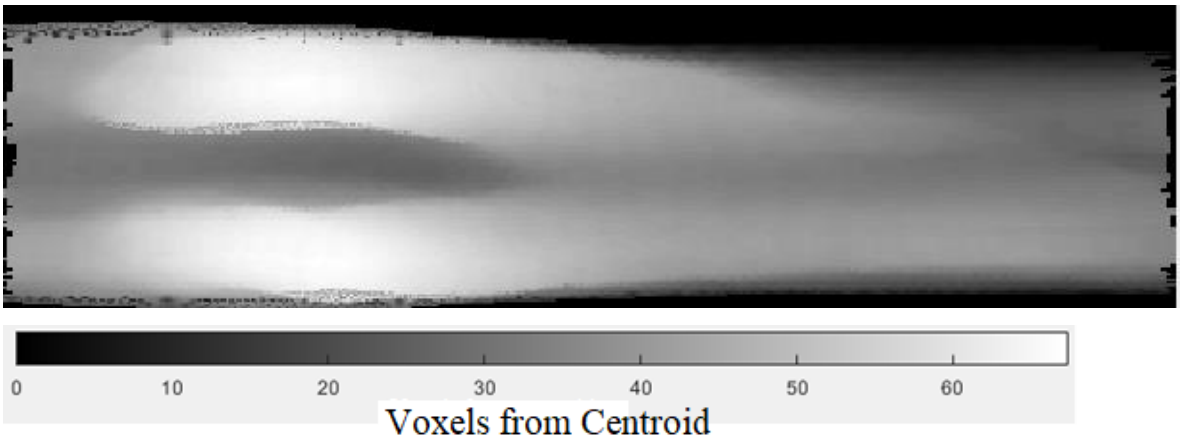

Figure 4-9 Sample 2D angular distance map in grayscale colormap

The distance maps have an important feature which is used to guide the subchondral region definition. The centroid point used in the map's generation is calculated from a sagittal slice not containing the condyles (the missing area in the 'shell image' in Figure 4-5A). In this slice, the anterior geometry remains relatively constant as one moves medially and laterally. Therefore, condylar voxels will always exhibit high distance values as they will be furthest from the calculated centroid. Adjusting the contrast and color map of the previously shown 2D angular distance map illustrates this approach (Figure 4-10). The posterior point at which there is a sharp drop in intensity (leftwards in Figure 4-10) can therefore be assumed to be the end of the condyle and correspondingly the end of the subchondral surface.

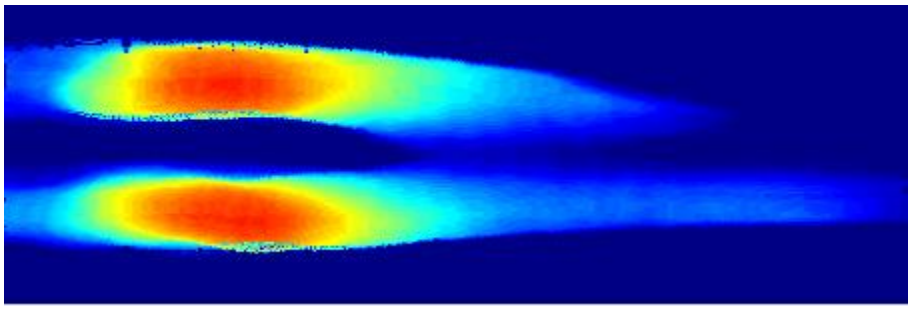

Figure 4-10 Contrasted sample 2D angular distance map in colormap jet

A region growing segmentation technique was used to locate the boundaries of these regions with the most posterior points used as the condylar end angles for the subchondral surface. However, anatomical variation in condyle curvature presents a challenge in having a set segmentation threshold. As a result, an experimentally found 'best-fit' value was used which can lead to underestimations of the true subchondral region (as estimated visually). The best-fit threshold errs on the side of underestimation, as for the purpose of density analyses, it is better to omit voxels which should be included than to include voxels which should not. Figure 4-11 provides an example where the set threshold value resulted in the underestimation of the true size of the subchondral surface (outlined in black). Additional information on the subchondral surface refinement methodology is provided in Appendix D.

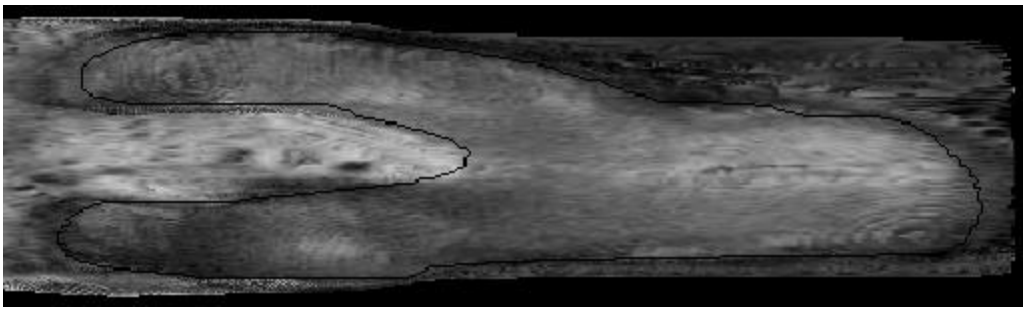

Figure 4-11 Outline of refined subchondral surface definition in a 2D angular BMD map. Specific image chosen to illustrate posterior end misalignment

After adjustments to the subchondral surface boundaries have been made in the 2D angular maps, the changes can then be converted and applied to the native 3D format, resulting in a completed subchondral surface definition. Figure 4-12 shows images of a refined subchondral surface volume.

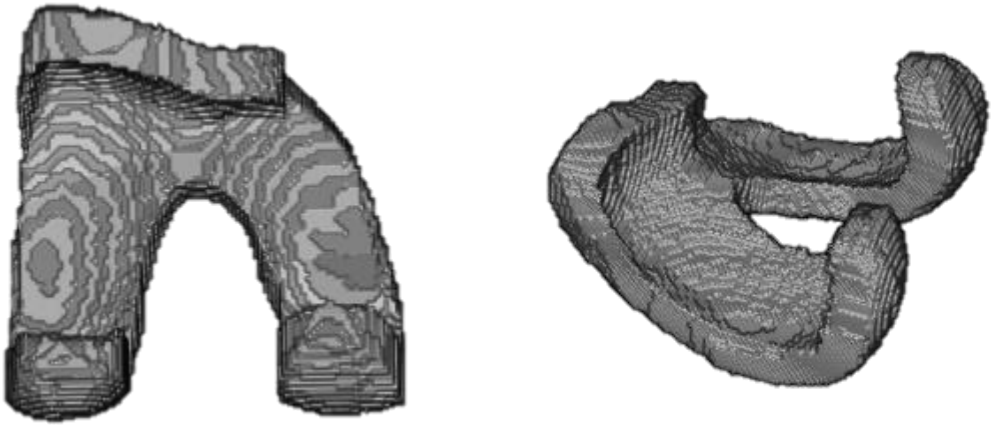

Figure 4-12 Refined subchondral surface volumes

4.7 Depth Definition

To account for the curvature of the distal femur, depth was assessed for each voxel via a process which can be conceptualized as ‘peeling off’ layers of the subchondral region. Therefore, depth in the context of this work is more aptly described as distance from the contact surface. This is noteworthy as voxels close to a mediolateral edge, such as condyle edges, are assigned a depth value based on their distance to the articulating surface, not the nearby edge of the condyle.

4.8 ROI Definition

Following similar works at the proximal tibia and patella [38, 53], the distal femur was divided into sub-regions of interest for analysis. This work employed two distinct ROI arrangements: The Pelletier ROI, and the MOAKS ROI. The Pelletier method was adapted from [54] in which cartilage volumes were separated into 7 regions: posterior, central and anterior condylar regions (for both medial and lateral) and an anterior trochlear region which includes the remaining volume. Figure 4-13 shows a diagram of the Pelletier ROI.

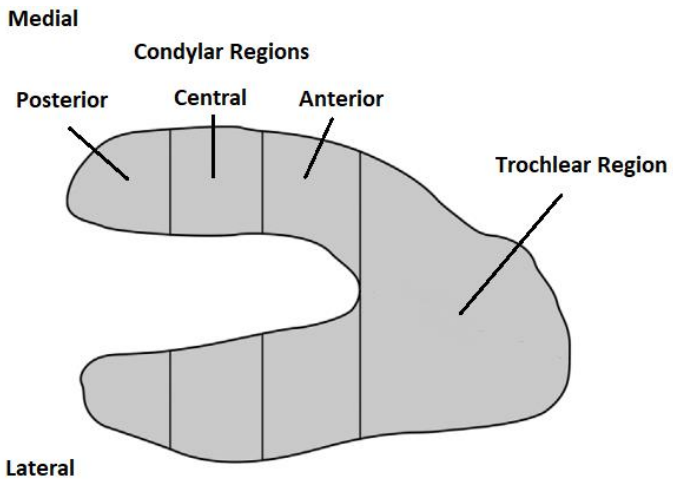

Figure 4-13 Pelletier ROI Diagram

The MOAKS ROI scheme is based on the eponymous approach for whole knee joint assessment [55]. There are 6 regions in the MOAKS ROI: posterior, central and anterior for both medial and lateral halves. Figure 4-14 shows a diagram of the MOAKS ROI. An additional MOAKS region was also investigated which modified the central medial region such that voxels near the intercondylar fossa (IF) area were removed. This was done as this region typically exhibits high densities caused by local ligament insertion sites. Since these high-density regions are not directly involved in tibial-femoral contact, they were hypothesized to be extraneous to this work. Figure 4-15A shows an example ROI where IF voxels have been included, highlighting the high-density voxels at this location. Figure 4-15B presents the modified MOAKS region with the shaded area being excluded from analysis. Appendix E provides additional information on how the ROIs were defined and applied to the distal femur.

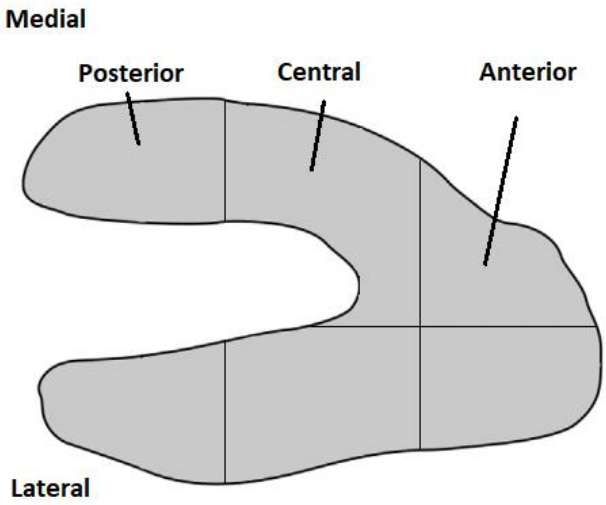

Figure 4-14 MOAKS ROI Diagram

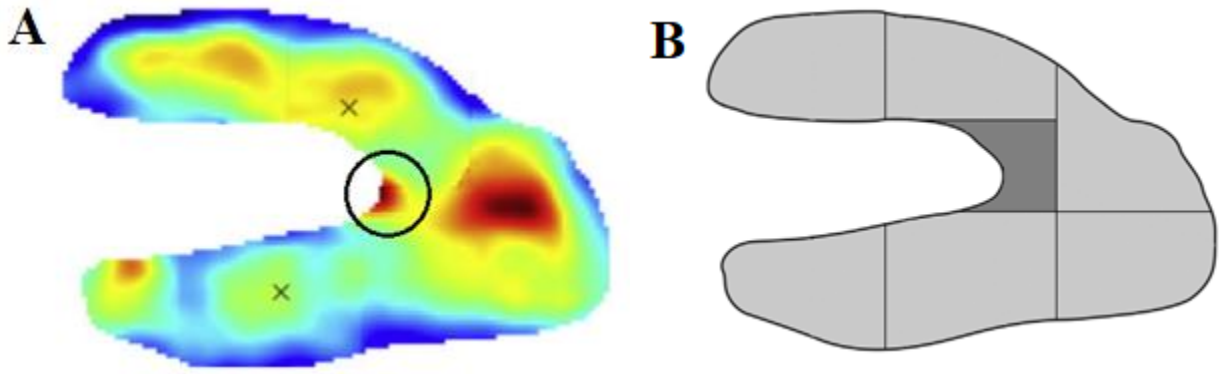

Figure 4-15 (A) Example ROI density projection exhibiting high-density intercondylar fossa voxels (B) Proposed modified central medial region with intercondylar fossa voxels removed

4.9 Peak Density Clusters

Following previous cluster based approaches in [43, 44, 53], clusters of the medial and lateral halves, in addition to each sub-region, were assessed for both ROI schemes. Instead of a threshold-based approach, this work opted for an analysis of the peak density cluster (PDC) found within each region. Due to difficulties in creating an appropriate cluster shape which accounts for the curved geometry of the distal femur, clusters were assessed in the 2D BMD maps instead.

Clusters were calculated as circular groupings of voxels and were assessed at depths between 0-2.5mm and 2.5-5mm. This depth range was chosen as it has been previously shown to

be the site of the largest differences between healthy and OA subchondral bone [38, 56].

The variation of cluster sizes between 3.125mm (5 voxels) to 9.375mm (15 voxels) was investigated, though general patterns were unaffected by this change. For brevity, only investigations using a cluster diameter of 5.625mm (9 voxels) were reported in this work.

4.10 Statistical Analysis

The precision (i.e., repeatability) of the regional BMD and peak cluster density measures was assessed via root mean square coefficients of variation ($CV\%_{RMS}$). $CV\%_{RMS}$ is calculated as described in [57] and is shown in Equation 4-1:

$$CV\%_{RMS} = \sqrt{\frac{\sum_{j=1}^{m}\left(\frac{SD_j}{\bar{x}_j}\times 100\%\right)^2}{m}}$$

Equation 4-1

where m is the number of participants, $\bar{x}_j$ is the mean of the repeated scans, and SD_j is the standard deviation of the repeated scans and is obtained from Equation 4-2:

$$SD_j = \sqrt{\frac{\sum_{i=1}^{n}\left(x_{ij} - \bar{x}_j\right)^2}{n-1}}$$

Equation 4-2

where n is the number of measurements performed, x_{ij} is the ith measurement for subject j. Precision errors were calculated for mean regional BMD measurements for depth groupings of 2.5mm (0-2.5mm, 2.5-5mm, 5-7.5mm). Similarly, precision errors were also calculated for clusters with the highest density for each region at depths between 0-2.5mm and 2.5-5mm.

This work had 28 degrees of freedom ($m * (n - 1) = 14 * (3 - 1) = 28$) for calculating precision. Following Glüer's recommendations in [57], this work exceeds the 27 degrees of freedom required to establish reliable precision errors. Specifically, 28 degrees of freedom results in an estimate of precision errors with an upper 90% confidence limit below 30% (i.e., a $CV\%_{RMS}$ = 2% has an upper 90% confidence limit of 2.60%). However, it should be noted that these calculations are representative of our mixed sample (i.e., combining the healthy and OA

groups) and valid only if both groups yield similar precision errors.

Mean regional BMD measurements, as well as peak density clusters, were compared between OA and normal knees. Student's t-tests were performed to compare between normally distributed measures while non-parametric Mann-Whitney U-tests were used for measures which were not normally distributed. The normality of each measure was assessed via the Shapiro-Wilk test. In cases where a single variable was 1.96 standard deviations from the mean, it was considered an outlier and removed from analysis. Where multiple tests were performed, the Benjamini-Hochberg procedure [58] was used to limit the false discovery rate (FDR).

Effect sizes were calculated and reported using Cohen's d. Post-hoc power calculations were done to provide an estimate of the sample sizes necessary to achieve adequate power (α = 0.05, power = 0.90) given the observed differences between OA and normal femora. Power calculations were performed for measurements that had large effect sizes (|Cohen's d|> 0.8).

CHAPTER 5
RESULTS

5.1 Precision

Precision data is reported using absolute values (root mean square standard deviation, SD_{RMS}) and by percentage (root mean square coefficients of variation, $CV\%_{RMS}$). Mean regional density $CV\%_{RMS}$ was low across all measurements, with precision errors ranging from 1.2% to 3.9% using the Pelletier ROI scheme (Table 5-1) and from 1.2% to 3.6% using the MOAKS ROI scheme (Table 5-2).

Peak density clusters at a depth of 0-2.5mm exhibited precision errors ranging from 1.4% to 10.6% for the Pelletier ROI (Table 5-3) and from 1.5% to 2.5% for the MOAKS ROI (Table 5-4). Conversely, at a depth between 2.5-5mm, $CV\%_{RMS}$ ranged from 1.3% to 9.1% for the Pelletier ROI scheme (Table 5-5) and from 1.6% to 3.6% for the MOAKS ROI scheme (Table 5-6).

Table 5-1 Precision results for mean regional BMD measures (mg/cm^3 K_2HPO_4) at depth groupings of 0-2.5mm, 2.5-5mm, and 5-7.5mm. Precision is reported using $CV\%_{RMS}$ for OA, healthy and total participants using the Pelletier ROI scheme

Region	Depth (mm)	First Scan		Second Scan		Third Scan		All Scans		CV%	CV% OA	CV% Healthy
		Mean	±SD	Mean	±SD	Mean	±SD	Mean	±SD			
Medial Posterior	0-2.5	416	83	413	80	418	85	415	82	2.8	3.1	2.4
	2.5-5	240	38	240	39	240	36	240	37	3.0	3.6	2.3
	5-7.5	200	33	196	34	197	33	198	33	3.1	4.0	1.8
Medial Central	0-2.5	477	81	465	78	481	86	474	81	2.5	2.8	2.1
	2.5-5	341	52	332	44	343	52	339	49	3.0	3.5	2.4
	5-7.5	306	49	299	38	305	50	303	45	3.0	4.0	1.6
Medial Anterior	0-2.5	497	112	495	117	499	112	497	113	2.1	2.2	2.0
	2.5-5	364	85	361	84	364	86	363	85	2.4	2.8	2.0
	5-7.5	300	76	302	77	299	77	300	76	2.2	2.5	1.8
Lateral Posterior	0-2.5	342	58	340	60	338	63	340	60	3.3	4.2	2.1
	2.5-5	213	51	210	50	209	51	211	50	3.4	4.2	2.2
	5-7.5	191	51	190	50	188	50	190	50	3.9	3.9	3.9
Lateral Central	0-2.5	373	54	370	51	371	52	371	52	1.9	2.1	1.6
	2.5-5	273	38	274	37	272	39	273	38	2.1	2.2	2.1
	5-7.5	248	40	248	38	247	39	248	39	1.8	2.2	1.5
Lateral Anterior	0-2.5	385	67	385	66	385	64	385	65	2.0	1.8	2.1
	2.5-5	292	49	294	49	291	48	292	48	1.7	1.7	1.6
	5-7.5	269	56	268	54	266	56	268	55	1.6	2.1	0.9
Anterior Central	0-2.5	446	58	449	59	447	57	447	58	1.6	1.8	1.4
	2.5-5	329	45	330	44	328	44	329	44	1.3	1.4	1.3
	5-7.5	283	52	282	51	281	50	282	51	1.2	1.0	1.3

Table 5-2 Precision results for mean regional BMD measures (mg/cm^3 K_2HPO_4) at depth groupings of 0-2.5mm, 2.5-5mm, and 5-7.5mm. Precision is reported using $CV\%_{RMS}$ for OA, healthy and total participants using the MOAKS ROI scheme

Region	Depth (mm)	First Scan		Second Scan		Third Scan		All Scans		CV%	CV% OA	CV% Healthy
		Mean	±SD	Mean	±SD	Mean	±SD	Mean	±SD			
Medial Posterior	0-2.5	454	82	449	81	458	87	454	83	1.8	1.9	1.7
	2.5-5	304	43	303	42	305	42	304	42	1.6	1.8	1.4
	5-7.5	268	42	267	38	265	38	266	39	2.2	2.8	1.1
Medial Central	0-2.5	491	93	491	93	492	92	491	92	1.7	2.1	1.3
	2.5-5	358	67	360	66	359	70	359	67	2.2	2.7	1.6
	5-7.5	288	54	289	55	287	55	288	55	1.7	1.7	1.7
Medial Anterior	0-2.5	471	54	467	57	473	55	470	55	2.1	2.2	2.0
	2.5-5	319	50	315	46	317	45	317	46	2.9	2.4	3.4
	5-7.5	251	57	247	53	251	53	250	54	3.6	2.8	4.3
Lateral Posterior	0-2.5	358	49	357	51	357	50	357	49	2.0	2.5	1.4
	2.5-5	247	37	247	39	246	40	247	39	1.7	2.1	1.2
	5-7.5	224	37	225	39	223	39	224	38	1.7	1.5	1.9
Lateral Central	0-2.5	390	61	395	60	387	57	391	59	2.3	2.3	2.3
	2.5-5	302	49	306	50	299	51	302	50	2.0	2.1	2.0
	5-7.5	285	58	286	59	282	60	285	59	1.6	1.9	1.3
Lateral Anterior	0-2.5	406	53	411	56	407	61	408	56	2.7	2.3	3.0
	2.5-5	310	38	309	33	309	39	309	36	2.3	1.5	2.9
	5-7.5	289	46	288	39	289	43	289	42	2.3	1.6	2.8

Table 5-3 Precision results for peak density cluster (PDC) (mg/cm^3 K_2HPO_4) analysis at combined depth groupings of 0-2.5mm. Precision is reported using $CV\%_{RMS}$ for OA, healthy and total participants using the Pelletier ROI

Region	First Scan		Second Scan		Third Scan		All Scans		CV%	CV% OA	CV% Healthy
	Mean	±SD	Mean	±SD	Mean	±SD	Mean	±SD			
Medial Half	709	116	719	121	718	130	715	118	5.5	2.4	7.4
Lateral Half	720	117	747	116	723	128	730	112	7.5	7.2	7.8
Medial Posterior	543	78	534	77	548	85	542	80	2.5	2.9	2.0
Medial Central	619	111	622	117	621	123	621	117	1.8	1.6	2.0
Medial Anterior	652	130	647	130	670	129	657	128	4.4	4.5	4.2
Lateral Posterior	477	55	473	71	474	63	474	62	3.3	4.5	1.2
Lateral Central	494	70	493	69	495	69	494	69	1.4	1.5	1.2
Lateral Anterior	574	129	567	128	572	130	571	116	10.6	13.1	7.2
Anterior Central	724	120	750	117	726	133	733	116	7.5	7.1	7.8

Table 5-4 Precision results for peak density cluster (PDC) (mg/cm^3 K_2HPO_4) analysis at combined depth groupings of 0-2.5mm. Precision is reported using $CV\%_{RMS}$ for OA, healthy and total participants using the MOAKS ROI

Region	First Scan		Second Scan		Third Scan		All Scans		CV%	CV% OA	CV% Healthy
	Mean	±SD	Mean	±SD	Mean	±SD	Mean	±SD			
Medial Half	709	116	719	121	718	130	715	118	5.5	2.4	7.4
Lateral Half	657	71	658	72	669	86	662	76	2.5	2.2	2.7
Medial Posterior	624	115	630	122	630	121	628	119	1.8	1.5	2.1
Medial Central	705	135	729	134	702	144	712	129	8.4	9.0	7.8
Medial Anterior	660	72	657	73	668	85	661	76	2.6	2.4	2.8
Lateral Posterior	507	68	506	71	507	66	506	68	1.5	1.1	1.8
Lateral Central	533	59	534	58	535	58	534	58	1.8	1.5	2.1
Lateral Anterior	566	62	571	63	573	72	570	65	2.0	1.8	2.1

Table 5-5 Precision results for peak density cluster (PDC) (mg/cm^3 K_2HPO_4) analysis at combined depth groupings of 2.5-5mm. Precision is reported using $CV\%_{RMS}$ for OA, healthy and total participants using the Pelletier ROI

Region	First Scan		Second Scan		Third Scan		All Scans		CV%	CV% OA	CV% Healthy
	Mean	±SD	Mean	±SD	Mean	±SD	Mean	±SD			
Medial Half	599	165	602	160	599	168	600	163	4.6	5.1	4.0
Lateral Half	590	174	580	163	581	169	584	168	2.0	2.3	1.7
Medial Posterior	345	49	345	51	344	53	345	49	5.1	6.5	3.1
Medial Central	506	129	503	127	508	130	506	128	1.3	1.8	0.5
Medial Anterior	539	148	517	130	549	151	535	138	7.3	4.0	9.5
Lateral Posterior	307	48	311	43	306	49	308	47	2.3	2.6	1.9
Lateral Central	368	44	373	44	368	45	370	44	2.5	1.6	3.2
Lateral Anterior	472	150	458	123	444	118	458	126	9.1	12.4	3.2
Anterior Central	604	175	608	161	601	178	604	170	5.2	5.2	5.1

Table 5-6 Precision results for peak density cluster (PDC) (mg/cm^3 K_2HPO_4) analysis at combined depth groupings of 2.5-5mm. Precision is reported using $CV\%_{RMS}$ for OA, healthy and total participants using the MOAKS ROI

Region	First Scan		Second Scan		Third Scan		All Scans		CV%	CV% OA	CV% Healthy
	Mean	±SD	Mean	±SD	Mean	±SD	Mean	±SD			
Medial Half	599	165	602	160	599	168	600	163	4.6	5.1	4.0
Lateral Half	522	100	509	78	508	83	513	86	3.1	1.6	4.0
Medial Posterior	510	129	505	128	509	129	508	129	2.3	1.1	3.0
Medial Central	592	175	595	167	591	179	593	172	5.8	6.1	5.5
Medial Anterior	516	104	502	86	500	90	506	93	3.6	2.9	4.3
Lateral Posterior	379	50	377	50	378	45	378	47	2.8	1.3	3.7
Lateral Central	471	57	467	63	464	61	467	60	2.6	1.6	3.3
Lateral Anterior	482	60	479	57	477	64	480	60	1.7	1.6	1.8

5.2 Mean Regional BMD measurements

Mean regional BMD measurements were calculated for both ROI schemes at depth grouping of 2.5mm (0-2.5, 2.5-5, 5-7.5mm). For all regions, there was a trend of decreasing mean regional BMD measurements with successively deeper layers. The first depth grouping, 0-2.5mm, exhibited higher densities than the other two (average regional density of 427 vs 302 and 262 mg/cm^3 K_2HPO_4) which can be explained by the presence of voxels containing cortical bone.

Regional density measures of the Pelletier ROI scheme (Table 5-7) exhibited a pattern where medial regions were 22% higher than lateral regions. Conversely, the regional density measures of the MOAKS ROI scheme (Table 5-8) showed medial regional density to be only 13% higher. This can be attributed to the Pelletier regions primarily capturing the tibiofemoral contact surface, amplifying the contrast of higher medial densities in these frequently loaded regions.

In total, 42 depth specific regions were assessed across the two ROI schemes ((7 MOAKS + 7 Pelletier regions) * 3 depth groupings). With the exception of the medial anterior region at depths of 2.5-5mm, no significant differences between groups were found. The Benjamini-Hochberg method strongly indicates that that the sole significant finding is likely to be a false positive. However, large percent differences (+15%) were found for many measurements, resulting in high Cohen's d scores.

General density patterns of the normal and OA distal femora were also qualitatively compared via density projection images created for each depth grouping (0-2.5, 2.5-5, 5-7.5mm). These images are presented in Figure 5-1.

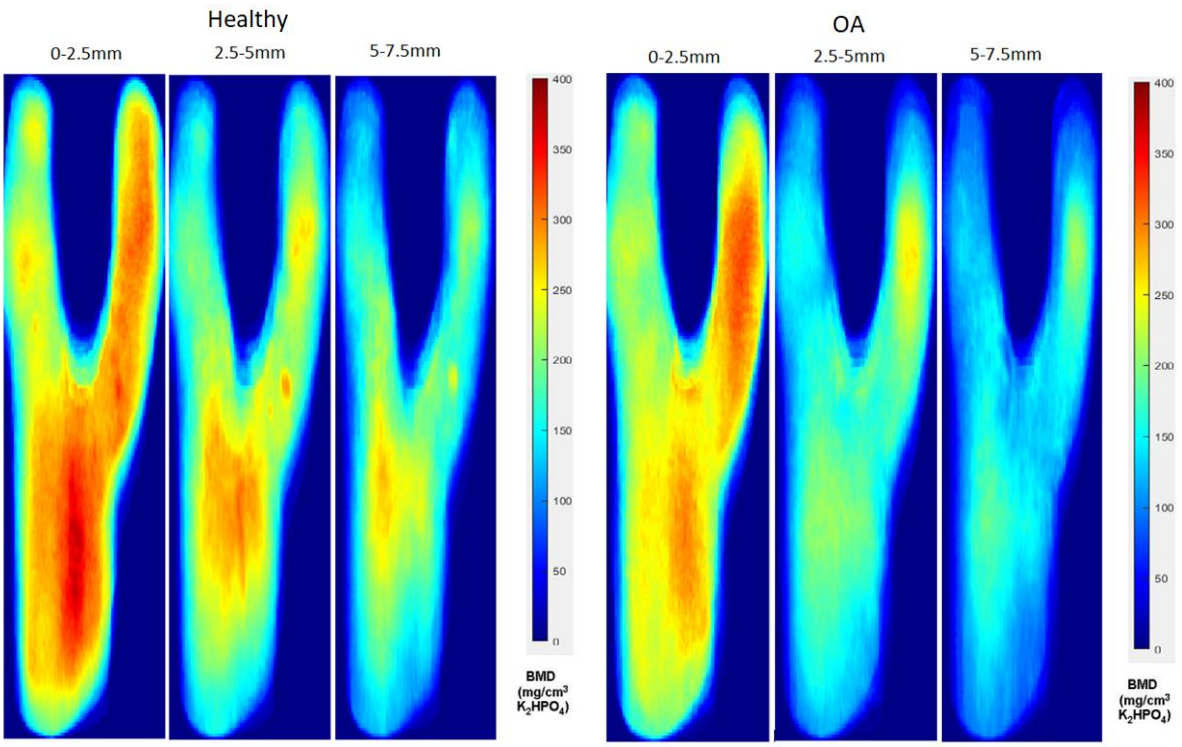

Figure 5-1 Representative topographical color maps of average distal femoral BMD at depths of 0-2.5mm, 2.5-5mm, and 5-7.5mm for healthy (left) and OA (right) participants

5.3 Peak Density Clusters

Peak density clusters were assessed for both ROI schemes and the resulting measurements were compared between healthy and OA knees at combined depths of 0-2.5mm (Table 5-9 for the Pelletier ROI and Table 5-10 for the MOAKS ROI) and 2.5-5mm (Table 5-11 for the Pelletier ROI and Table 5-12 for the MOAKS ROI).

Using the MOAKS ROIs, peak density clusters were found to be 18%, 19% and 12% lower for the OA group in the lateral half, medial anterior and lateral anterior regions respectively at combined depths of 2.5-5mm. However, despite three of eight regions appearing to differ significantly between normal and OA distal femora, the Benjamini-Hochberg procedure indicates these findings are false positives. This result should be taken with care as the limited sample size of this study likely precludes high confidence in any measured difference, resulting in their likely invalidation using FDR techniques. Aside from these findings, no significant differences were detected.

Table 5-7 Mean BMD (mg/cm^3 K_2HPO_4) ± standard deviation (SD), absolute and percent difference between OA and normal participants, and Cohen's d effect size for depth groupings of 0-2.5mm, 2.5-5mm, and 5-7.5mm using the Pelletier ROI scheme. Significant findings prior to FDR application are bolded; no findings remained significant following FDR corrections.

Region		OA		Normal		Difference		%Difference / $CV\%_{RMS}$	Cohen's d	P-value
	Depth (mm)	Mean BMD	SD	Mean BMD	SD	Absolute	Percent			
Medial Posterior	0-2.5	426	97	405	60	22	0.3	2.0	0.3	0.64
	2.5-5	221	34	259	30	-38	-1.2	-4.9	-1.2	0.06
	5-7.5	183	27	212	32	-29	-1.0	-4.5	-1.0	0.10
Medial Central	0-2.5	512	87	436	49	76	1.1	7.1	1.1	0.08
	2.5-5	347	62	330	30	17	0.4	1.7	0.4	0.53
	5-7.5	314	55	293	29	21	0.5	2.3	0.5	0.42
Medial Anterior	0-2.5	549	131	445	49	104	1.1	11.3	1.1	0.09
	2.5-5	388	106	339	41	49	0.6	5.9	0.6	0.30
	5-7.5	325	95	276	35	48	0.7	7.9	0.7	0.25
Lateral Posterior	0-2.5	337	53	343	65	-6	-0.1	-0.5	-0.1	0.88
	2.5-5	190	43	231	47	-40	-0.9	-5.3	-0.9	0.14
	5-7.5	173	45	207	48	-34	-0.7	-4.3	-0.7	0.26
Lateral Central	0-2.5	385	54	358	45	27	0.5	4.1	0.5	0.34
	2.5-5	265	31	281	41	-15	-0.4	-2.7	-0.4	0.47
	5-7.5	238	33	258	41	-21	-0.6	-4.9	-0.6	0.33
Lateral Anterior	0-2.5	404	70	365	51	39	0.6	5.8	0.6	0.27
	2.5-5	282	43	303	50	-21	-0.4	-4.1	-0.4	0.45
	5-7.5	249	44	287	57	-38	-0.7	-9.2	-0.7	0.21
Anterior Central	0-2.5	458	60	437	53	20	0.4	2.9	0.4	0.53
	2.5-5	309	34	348	43	-39	-1.0	-8.3	-1.0	0.10
	5-7.5	261	34	303	54	-43	-0.9	-12.1	-0.9	0.12

Table 5-8 Mean BMD (mg/cm^3 K_2HPO_4) ± standard deviation (SD), absolute and percent difference between OA and normal participants, and Cohen's d effect size for depth groupings of 0-2.5mm, 2.5-5mm, and 5-7.5mm using the MOAKS ROI scheme. Significant findings prior to FDR application are bolded; no findings remained significant following FDR corrections.

Region	Depth (mm)	OA		Normal		Difference		%Difference / $CV\%_{RMS}$	Cohen's d	P-value
		Mean BMD	SD	Mean BMD	SD	Absolute	Percent			
Medial Posterior	0-2.5	486	93	422	53	64	15	8.4	0.8	0.16
	2.5-5	309	53	300	25	9	3	1.9	0.2	0.70
	5-7.5	273	48	260	26	13	5	2.3	0.3	0.55
Medial Central	0-2.5	519	105	463	63	55	12	6.0	0.6	0.28
	2.5-5	356	79	362	52	-5	-1	2.4	-0.1	0.89
	5-7.5	283	56	294	52	-11	-4	5.1	-0.2	0.72
Medial Anterior	0-2.5	473	41	468	65	5	1	0.5	0.1	0.88
	2.5-5	**292**	**39**	**342**	**39**	**-50**	**-15**	**-5.0**	**-1.3**	**0.04**
	5-7.5	228	46	271	52	-42	-16	-4.3	-0.9	0.15
Lateral Posterior	0-2.5	366	45	349	51	18	5	2.5	0.4	0.53
	2.5-5	235	30	258	42	-23	-9	-5.1	-0.6	0.28
	5-7.5	212	32	236	39	-24	-10	-6.1	-0.7	0.25
Lateral Central	0-2.5	408	60	374	51	35	9	3.9	0.6	0.46
	2.5-5	284	42	320	50	-36	-11	-5.5	-0.8	0.19
	5-7.5	260	45	309	59	-49	-16	-9.7	-0.9	0.13
Lateral Anterior	0-2.5	424	66	392	38	32	8	3.1	0.6	0.30
	2.5-5	299	34	319	36	-20	-6	-2.7	-0.6	0.32
	5-7.5	275	27	302	49	-27	-9	-3.9	-0.7	0.24

Table 5-9 Mean peak density cluster (PDC) (mg/cm^3 K_2HPO_4) ± standard deviation (SD), absolute and percent difference between OA and normal participants, and Cohen's d effect size for combined depth groupings of 0-2.5mm using the Pelletier ROI. Significant findings prior to FDR application are bolded; no findings remained significant following FDR corrections.

Region	OA		Normal		Difference		%Difference / CV%$_{RMS}$	Cohen's d	P-value
	Mean PDC	SD	Mean PDC	SD	Absolute	Percent			
Medial Half	738	117	693	121	45	6	1.2	0.4	0.50
Lateral Half	745	110	715	126	29	4	0.5	0.2	0.65
Medial Posterior	554	89	529	67	25	5	0.5	0.3	0.59
Medial Central	674	129	567	63	107	19	1.9	1.1	0.08
Medial Anterior	706	138	607	95	99	16	10.3	0.8	0.16
Lateral Posterior	474	70	475	55	-2	0	3.7	0.0	0.94
Lateral Central	501	72	487	64	15	3	-0.1	0.2	0.72
Lateral Anterior	594	136	548	113	46	8	2.1	0.4	0.46
Anterior Central	751	116	716	126	35	5	0.8	0.3	0.59

Table 5-10 Mean peak density cluster (PDC) (mg/cm^3 K_2HPO_4) ± standard deviation (SD), absolute and percent difference between OA and normal participants, and Cohen's d effect size for combined depth groupings of 0-2.5mm using the MOAKS ROI. Significant findings prior to FDR application are bolded; no findings remained significant following FDR corrections.

Region	OA		Normal		Difference		%Difference / CV%$_{RMS}$	Cohen's d	P-value
	Mean PDC	SD	Mean PDC	SD	Absolute	Percent			
Medial Half	738	117	693	121	45	6	1.2	0.4	0.50
Lateral Half	745	110	715	126	29	4	0.5	0.2	0.65
Medial Posterior	682	135	575	61	107	19	10.0	1.0	0.09
Medial Central	750	128	674	134	76	11	1.3	0.6	0.29
Medial Anterior	658	52	671	95	-13	-2	-0.8	-0.2	0.77
Lateral Posterior	510	74	503	60	8	2	1.0	0.1	0.84
Lateral Central	555	65	545	66	11	2	0.9	0.2	0.77
Lateral Anterior	580	63	561	68	20	3	1.7	0.3	0.60

Table 5-11 Mean peak density cluster (PDC) (mg/cm^3 K_2HPO_4) ± standard deviation (SD), absolute and percent difference between OA and normal participants, and Cohen's d effect size for combined depth groupings of 2.5-5mm using the Pelletier ROI. Significant findings prior to FDR application are bolded; no findings remained significant following FDR corrections.

Region	OA		Normal		Difference		%Difference / CV%$_{RMS}$	Cohen's d	P-value
	Mean PDC	SD	Mean PDC	SD	Absolute	Percent			
Medial Half	526	64	598	119	-72	-12	-2.6	-0.8	0.21
Lateral Half	508	91	582	113	-74	-13	-6.3	-0.7	0.23
Medial Posterior	322	39	367	50	-45	-12	-2.4	-1.0	0.08
Medial Central	479	88	474	50	5	1	0.9	0.1	0.89
Medial Anterior	487	84	526	109	-39	-7	-1.0	-0.4	0.49
Lateral Posterior	**284**	**46**	**332**	**35**	**-48**	**-15**	**-6.3**	**-1.2**	**0.05**
Lateral Central	358	40	382	47	-24	-6	-2.5	-0.6	0.32
Lateral Anterior	416	69	443	84	-27	-6	-0.7	-0.3	0.55
Anterior Central	523	83	610	128	-87	-14	-2.7	-0.8	0.18

Table 5-12 Mean peak density cluster (PDC) (mg/cm^3 K_2HPO_4) ± standard deviation (SD), absolute and percent difference between OA and normal participants, and Cohen's d effect size for combined depth groupings of 2.5-5mm using the MOAKS ROI. Significant findings prior to FDR application are bolded; no findings remained significant following FDR corrections.

Region	OA		Normal		Difference		%Difference / CV%$_{RMS}$	Cohen's d	P-value
	Mean PDC	SD	Mean PDC	SD	Absolute	Percent			
Medial Half	526	64	598	119	-72	-12	-2.6	-0.8	0.21
Lateral Half	508	91	582	113	-74	-13	-4.1	-0.7	0.23
Medial Posterior	488	91	470	45	18	4	1.6	0.2	0.66
Medial Central	529	96	539	69	-10	-2	-0.3	-0.1	0.83
Medial Anterior	**453**	**42**	**565**	**102**	**-112**	**-20**	**-5.5**	**-1.4**	**0.02**
Lateral Posterior	363	36	402	56	-39	-10	-3.5	-0.8	0.14
Lateral Central	444	27	511	82	-67	-13	-5.0	-1.1	0.08
Lateral Anterior	**448**	**33**	**512**	**68**	**-64**	**-12**	**-7.3**	**-1.2**	**0.05**

5.4 Post-hoc Power Analysis

Statistical power analyses were done to estimate how many subjects would be required to differentiate between OA and normal distal femora in cases where effect size was found to be large (|Cohen's D| > 0.8). Using power analysis parameters of $\alpha = 0.05$ and power = 0.80, 26 samples per group were found to be required to differentiate measures which exhibited large effect sizes.

CHAPTER 6
DISCUSSION

6.1 Overview of Findings

Both OA and healthy groups exhibited similar precision errors, therefore justifying the decision to combine groups in order to achieve adequate degrees of freedom for precision assessment. The *in vivo* precision at the distal femur is similar to those previously reported at the proximal tibia [53] and at the patella [38]. Table 6-1 compares the range of *in vivo* precisions at various depths for each of these investigations.

Table 6-1 Comparison of precision errors ($CV\%_{RMS}$) between similar studies at the distal femur, proximal tibia and patella

	$CV\%_{RMS}$		
Depth (mm)	Distal Femur (MOAKS ROI)	Proximal Tibia [53]	Patella [38]
0 - 2.5	1.8 - 2.7	0.9 - 3.9	1.1 - 6.8
2.5 - 5	1.6 - 2.9	1.6 - 4.0	1.2 - 5.0
5 - 7.5	1.6 - 3.6	*1.5 - 3.0	1.6 - 5.1
*5 - 10			

One trend which was expected, but not observed was a decrease in precision error as depth increased (average precision errors did not vary by more than 0.1% across all depth measures). Generally, density patterns diminish as depth increases, theoretically minimizing precision errors associated with incorrect positioning and ROI definition. However, since this trend was not observed, it could indicate the workflow has errors which accumulate with increasing depth, balancing precision error across all depths.

There were no substantial variations in precision between most regions in either ROI scheme when assessing mean regional BMD. However, peak density cluster precision was noticeably lower in regions containing the high-density voxels belonging to the intercondylar fossa area (the Pelletier medial and lateral condylar anterior regions and the medial central MOAKS region). The medial and lateral anterior Pelletier regions had average $CV\%_{RMS}$ values of 5.9% and 9.8% respectively (the average regional $CV\%_{RMS}$ for all regions was 4.6%).

Similarly, the MOAKS medial central region exhibited a $CV\%_{RMS}$ of 7.1%, much higher than the average regional $CV\%_{RMS}$ of 3.3%. Comparing the precision at this area with the modified region where IF voxels were removed provides further evidence that these voxels can lead to increased precision error. Table 6-2 provides a comparison between the regions with and without the IF voxels.

Table 6-2 Comparison of peak density cluster precision errors ($CV\%_{RMS}$) between the unmodified MOAKS regions containing intercondylar fossa (IF) voxels and modified regions with the IF area removed

	$CV\%_{RMS}$	
Depth (mm)	Unmodified	IF area removed
Medial Half		
0-2.5	5.5	2.2
2.5-5	4.6	1.6
Medial Central		
0-2.5	8.4	1.7
2.5-5	5.8	2.4

Across all regions near the IF area, the $CV\%_{RMS}$ values of the modified regions are lower than their unmodified counterparts. Investigating this finding further yielded that these larger precision errors were the result of instances where a sufficient cluster volume of IF voxels were present in some, but not all of the repeated scans and resulting region definitions. This led to some peak density cluster values which far exceeded those in which the IF voxels were not present, resulting in precision errors above 23%. Though this issue is a result of a region definition error, it highlights the pronounced effect the IF voxels can have if not properly accounted for. With all fully automated workflows of this nature, small errors in region definition are unavoidable; however, methodologies which specifically account for these high-density voxels may be a superior approach.

As a focal point of this work is to assess joint mechanics and the resulting density distributions, accounting for the elevated densities seen in the IF region could be a critical step in eliminating noise which obfuscates underlying patterns from joint contact. This is particularly crucial for research investigating relationships between subchondral bone and articular cartilage, as the IF voxels may not be significantly affected by contact forces and cartilage quality, though

their inclusion could skew density measurements. Similarly, investigations of peak densities should also give careful consideration to the inclusion of the IF voxels as they can consistently exhibit densities well above those found elsewhere in the subchondral region.

Mean BMD measures did not appear to vary significantly between OA and healthy groups. However, large effect sizes prompted post-hoc power analyses to estimate a future sample size which may yield significance if similar effect size trends persist (n = 52, 26 per group). Conversely, peak density cluster measures at depths of 2.5-5mm did appear to vary between OA and healthy distal femora when using the MOAKS ROI scheme. Both lateral and medial anterior regions were observed to have significantly lower peak cluster densities for individuals with OA. One possible explanation for these findings is that OA associated cartilage degeneration at normal physiologic loading sites could lead to redistributed joint loading such that force is transferred relatively widely across the contact surface, resulting in a more dispersed density pattern. Conversely, individuals suffering from OA-related pain may be less active, resulting in reduced bone loading and subsequent bone remodeling compared to healthy participants. This is somewhat supported by the density projections shown in Figure 5-1 where the OA group appeared to have fewer areas of high-density bone, suggesting loading may be distributed more evenly in those with OA. Lastly, it should be noted that despite achieving statistical significance, the Benjamini-Hochberg procedure indicated these findings are likely to be false positives. However, this should be taken with care as the Benjamini-Hochberg method is conservative, and this study is likely to be underpowered due to its small participant size.

The results also offer insight into the general performance of both ROIs used in this work. The precision error of the MOAKS regions were typically lower than those of the Pelletier regions. Average precision errors were lower for every observed analysis in the MOAKS ROI compared with the Pelletier ROI (Mean regional BMD: 2.2% vs 2.4%, PDC at 0-2.5mm: 2.0% vs 4.9%, PDC at 2.5-5mm: 2.5% vs 4.4%). Additionally, no significant differences were observed between healthy and OA distal femora when using the Pelletier ROI scheme. It therefore may be reasonable to conclude that the MOAKS ROI is superior to the Pelletier ROI for the partitioning of sub-regions of the distal femur for BMD assessments.

6.2 Study Strengths

This thesis research had various strengths which highlight the usefulness and novelty of this work. Specifically, this research made use of a novel method to organize and display the volumetric BMD data of the distal femur via 2D angular projection maps. This is useful at the distal femur as the surface is continuously curved, creating challenges in defining uniform cluster shapes and assigning surface depths. Additionally, this 2nd view allows for supplementary methods to subjectively assess the relative 'fit' of the delineated subchondral region.

This work also investigated two distinct ROI schemes in order to independently investigate their respective utility. This had two important advantages:

- Precision of the workflow was independently verified for both ROI schemes. Differences between the ROIs provided insight into the strengths and weaknesses of the workflow and allowed for greater sensitivity in locating possible future improvements (e.g., poor precision of the posterior regions of the Pelletier scheme indicated this area was prone to error)
- By contrasting the results of both ROI schemes, their respective strengths and weaknesses, as well as their general utility in differentiating normal and OA distal femora, was elucidated

This work also succeeded in its objective of developing a fully automated workflow (post-segmentation) to assess regional depth-specific subchondral BMD. The assessed precision of this workflow was similar to non-automated investigations at the proximal tibia and patella [38, 53]. An additional benefit of automating this work is the removal of human error, both from inter-observer and intra-observer variability, leading to more consistent results. Lastly, this research had sufficient participants and repeated scans to exceed the 27 degrees of freedom recommended by [57] to achieve conservative precision errors with small confidence intervals (upper 90% confidence interval of below 30%).

6.3 Study Limitations

This research had various limitations related to study sample size, study design and limitations of the workflow used. First, although this work had a sufficient number of patient scans for

precision purposes, this study may have been underpowered to determine differences between normal and OA distal femoral BMD measures. In general, large effect sizes (|Cohen's d| > 0.8) between normal and OA BMD measures are required for clinical significance, necessitating higher powered studies. This work had only 7 subjects per group which may not have been sufficient to achieve an adequately powered study.

A second limitation of this work relates to the method in which normal and OA density measures were compared. Both regional and peak cluster densities can be affected by several factors, many of which are challenging to account for (valgus/varus alignment, cyst presence, varying loading patterns, etc.). These confounding variables were not accounted for in this work, which may obfuscate possible underlying density variations between normal and OA distal femora. This limitation highlights the importance of applying these methods to larger datasets which will diminish the statistical effect these confounding variables will have.

Another limitation of this work is the lack of validation for the accuracy of the developed workflow. No gold standard subchondral region definition was created for this research, impeding objective assessments of the final defined ROI and corresponding BMD measures. Visualizing the subchondral overlay for both native 3D and 2D maps aid in subjectively determining the fit of the ROIs; however, this does not provide any quantitative measures on accuracy. Other works addressed this limitation by using supplementary MRI imaging or arthrography to incorporate cartilage location to inform subchondral bone placement [59, 60]. However, this process necessitates additional imaging, manual cartilage segmentation, and registration techniques to achieve this. Alternatively, this limitation could be addressed in a future study in which a trained operator manually defines the subchondral region which is then compared with the region defined via automated methods. This would provide an objective method to evaluate the accuracy of the developed workflow without the need of MRI imaging.

CHAPTER 7
CONCLUSION AND FUTURE WORK

7.1 Conclusions

The objectives of this work were to: 1) develop an automated image processing algorithm for assessing regional and depth-specific BMD measures at the distal femur; 2) determine precision errors of the depth-specific distal femoral density measures; and 3) investigate differences in regional distal femoral density measures between individuals with and without knee OA

Objective 1 was met as the developed workflow is capable of assessing regional and depth-specific BMD measures (mean BMD and peak density clusters) without human involvement. Though a quantitative evaluation of accuracy was not included in this work, subjective assessment of the relative 'fit' of the defined ROI indicates the workflow has modest accuracy.

Precision errors were calculated and reported for each region at three depth groupings (0-2.5, 2.5-5, 5-7.5mm), satisfying Objective 2. Mean regional precision errors ranged from 1.2% to 3.9% with an average of 2.3% while peak density cluster precision ranged from 1.6% to 9.1% with an average of 3.7%.

Regional density measures were compared between healthy and OA knees for two ROI schemes via student's t-tests. No significant differences were detected. Though, where large effect sizes were found, power analyses were done to estimate the number of participants needed to achieve significance for future studies if effect sizes persisted. The analysis indicated that 26 subjects per group would be necessary to differentiate between groups for density measures with large effect sizes (|Cohen's d| > 0.8).

Peak density clusters were also compared for both ROI schemes via t-tests. Two regions in the MOAKS ROI scheme were found to have significantly different peak densities between healthy and normal knees. However, conservative false discovery rate techniques indicate these findings may be type I errors (false positives). Despite this, it is possible that this research was too underpowered to overcome the false discovery rate corrections and that these findings may warrant future investigation.

7.2 Contributions

The primary contribution of this work is the generation of a novel workflow which automates several tasks required for BMD assessments at the distal femur such as: orientation and alignment of 3D segmented distal femur objects, delineation of an estimated subchondral surface from surrounding bone, division of the subchondral surface into predefined ROI schemes, and regional and depth-specific assessments of mean density and peak cluster density measures. By automating these tasks, it is estimated that 10 minutes of human involvement per scan can be eliminated, saving upwards of 8 weeks of manual labour when applied to a dataset comprised of 2000 samples.

This work also contributed insights into the optimization of methods and design choices for similar future investigations such as:

- Pros and cons of the Pelletier and MOAKS ROI schemes
- The effects of removing intercondylar fossa voxels
- The use of 2D BMD maps for subchondral region delineation
- Power analyses to guide sample size choice for future work

7.3 Future Research

1. The accuracy of this work could be assessed in a future study in which the subchondral region and associated BMD values are manually determined from the QCT volumes. This would require slight approximations as the subchondral region is formally defined based on cartilage location, information not available through QCT alone. Alternatively, datasets comprised of both QCT and MRI imaging or CT arthrogram imaging could be utilized to address this limitation and provide a ground truth subchondral region. This would be achieved via the segmentation of cartilage from the MRI or CT arthrogram volumes followed by a co-registration of the cartilage volume onto the QCT volume. The resulting overlap would create a trustworthy subchondral region which can then be used to assess the automated workflow accuracy.
2. A major step of the developed workflow is to delineate the subchondral region from the surrounding bone. This process may have applications in finite element modeling (FEM) research where soft tissues such as cartilage are included. Cartilage is indiscernible in

clinical CT imaging, requiring supplemental MRI imaging or arthrography to properly model. However, cartilage morphology can be inferred based on the subchondral bone morphology, if known. This approach could be validated by comparing this inferred cartilage morphology to one found via MRI segmentation and co-registration (similar to above). Once validated, this application could aid in cartilage modeling for FEM studies where MRI imaging is not available.

3. Despite achieving suitable precision, further workflow refinement could lead to improved precision and accuracy which may allow for the use of smaller ROIs. Smaller ROIs could be advantageous as they may be necessary to locate density patterns too subtle to detect with the ROIs currently used. One obvious avenue for workflow refinement is more sophisticated use of automatic segmentation. Basic segmentation techniques are currently used to help guide ROI boundaries, however, more advanced and application specific techniques could be leveraged to achieve better outcomes for this end.
4. A significant advantage of creating a fully automated workflow is to allow for a seamless application to larger datasets. Research involving larger datasets will typically have higher statistical power and allow for greater insights into population differences by reducing the effect of confounding variables. The workflow developed as part of this research could be applied to larger datasets such as the Multicenter Osteoarthritis Study or Osteoarthritis Initiative datasets for such ends. Similarly, QCT datasets which also include additional categorical information such as WOMAC pain scores could be assessed in future work to explore relationships between subchondral BMD measures and patient reported clinical symptom expression.

LIST OF REFERENCES

[1] D. J. Hunter and D. T. Felson, "Osteoarthritis," (in eng), *BMJ*, vol. 332, no. 7542, pp. 639-42, Mar 2006, doi: 10.1136/bmj.332.7542.639.

[2] D. T. Felson *et al.*, "Osteoarthritis: new insights. Part 1: the disease and its risk factors," *Ann Intern Med*, vol. 133, no. 8, pp. 635-46, Oct 17 2000.

[3] P. H. A. o. Canada. "Osteoarthritis in Canada." https://www.canada.ca/en/public-health/services/publications/diseases-conditions/osteoarthritis.html (accessed September 14th, 2022, 2022).

[4] B. Sharif, R. Garner, D. Hennessy, C. Sanmartin, W. M. Flanagan, and D. A. Marshall, "Productivity costs of work loss associated with osteoarthritis in Canada from 2010 to 2031," (in eng), *Osteoarthritis Cartilage*, vol. 25, no. 2, pp. 249-258, 02 2017, doi: 10.1016/j.joca.2016.09.011.

[5] D. J. Hunter, J. J. McDougall, and F. J. Keefe, "The symptoms of osteoarthritis and the genesis of pain," (in eng), *Rheum Dis Clin North Am*, vol. 34, no. 3, pp. 623-43, Aug 2008, doi: 10.1016/j.rdc.2008.05.004.

[6] P. Dieppe, "Subchondral bone should be the main target for the treatment of pain and disease progression in osteoarthritis," (in eng), *Osteoarthritis Cartilage*, vol. 7, no. 3, pp. 325-6, May 1999, doi: 10.1053/joca.1998.0182.

[7] N. Bellamy, W. W. Buchanan, C. H. Goldsmith, J. Campbell, and L. W. Stitt, "Validation study of WOMAC: a health status instrument for measuring clinically important patient relevant outcomes to antirheumatic drug therapy in patients with osteoarthritis of the hip or knee," *J Rheumatol*, vol. 15, no. 12, pp. 1833-40, Dec 1988.

[8] M. D. Kohn, A. A. Sassoon, and N. D. Fernando, "Classifications in Brief: Kellgren-Lawrence Classification of Osteoarthritis," (in eng), *Clin Orthop Relat Res*, vol. 474, no. 8, pp. 1886-93, Aug 2016, doi: 10.1007/s11999-016-4732-4.

[9] M. T. Hannan, D. T. Felson, and T. Pincus, "Analysis of the discordance between radiographic changes and knee pain in osteoarthritis of the knee," (in eng), *J Rheumatol*, vol. 27, no. 6, pp. 1513-7, Jun 2000.

[10] D. B. Burr and M. B. Schaffler, "The involvement of subchondral mineralized tissues in osteoarthrosis: quantitative microscopic evidence," *Microsc Res Tech*, vol. 37, no. 4, pp. 343-57, May 15 1997.

[11] X. Mao, C. Chen, B. Wang, J. Hou, and C. Xiang, "A global bibliometric and visualized analysis in the status and trends of subchondral bone research," (in eng), *Medicine (Baltimore)*, vol. 99, no. 22, p. e20406, May 2020, doi: 10.1097/MD.0000000000020406.

[12] A. J. Bailey and J. P. Mansell, "Do subchondral bone changes exacerbate or precede articular cartilage destruction in osteoarthritis of the elderly?," *Gerontology vol.* 43, no. 5, pp. 296-304, 1997.

[13] E. L. Radin and J. L. Paul, "Importance of Bone in Sparing Articular Cartilage from Impact," *Clinical Orthopaedics and Related Research,* vol. 78, pp. 342-344, 1971.

[14] B. Helgason, E. Perilli, E. Schileo, F. Taddei, S. Brynjolfsson, and M. Viceconti, "Mathematical relationships between bone density and mechanical properties: a literature review," *Clin Biomech (Bristol, Avon),* vol. 23, no. 2, pp. 135-46, Feb 2008.

[15] E. Lammentausta, M. A. Hakulinen, J. S. Jurvelin, and M. T. Nieminen, "Prediction of mechanical properties of trabecular bone using quantitative MRI," *Physics in Medicine and Biology*, vol. 51, no. 23, pp. 6187-6198, 2006-12-07 2006, doi: 10.1088/0031-9155/51/23/017.

[16] W. D. Burnett *et al.*, "Knee osteoarthritis patients with severe nocturnal pain have altered proximal tibial subchondral bone mineral density," (in eng), *Osteoarthritis Cartilage,* vol. 23, no. 9, pp. 1483-90, Sep 2015, doi: 10.1016/j.joca.2015.04.012S1063-4584(15)01132-2 [pii].

[17] W. Burnett *et al.*, "Patella bone density is lower in knee osteoarthritis patients experiencing moderate-to-severe pain at rest," (in eng), *J Musculoskelet Neuronal Interact,* vol. 16, no. 1, pp. 33-9, Mar 2016.

[18] T. Neogi, "Clinical significance of bone changes in osteoarthritis," (in eng), *Ther Adv Musculoskelet Dis,* vol. 4, no. 4, pp. 259-67, Aug 2012, doi: 10.1177/1759720X1243735410.1177_1759720X12437354 [pii].

[19] Y. Zhang and J. M. Jordan, "Epidemiology of osteoarthritis," (in eng), *Clin Geriatr Med,* vol. 26, no. 3, pp. 355-69, Aug 2010, doi: 10.1016/j.cger.2010.03.001.

[20] G. Wu *et al.*, "ISB recommendation on definitions of joint coordinate system of various joints for the reporting of human joint motion--part I: ankle, hip, and spine. International Society of Biomechanics," (in eng), *J Biomech,* vol. 35, no. 4, pp. 543-8, Apr 2002, doi: 10.1016/s0021-9290(01)00222-6.

[21] M. C. M. Fischer, S. A. G. A. Grothues, J. Habor, M. de la Fuente, and K. Radermacher, "A robust method for automatic identification of femoral landmarks, axes, planes and bone coordinate systems using surface models," (in eng), *Sci Rep,* vol. 10, no. 1, p. 20859, 11 2020, doi: 10.1038/s41598-020-77479-z.

[22] K. Li, S. Tashman, F. Fu, C. Harner, and X. Zhang, "Automating analyses of the distal femur articular geometry based on three-dimensional surface data," (in eng), *Ann Biomed Eng,* vol. 38, no. 9, pp. 2928-36, Sep 2010, doi: 10.1007/s10439-010-0064-9.

[23] L. Hirtler, F. Kainberger, and S. Röhrich, "The intercondylar fossa—A narrative review," *Clinical Anatomy,* vol. 35, no. 1, pp. 2-14, 2022-01-01 2022, doi: 10.1002/ca.23773.

[24] S. R. Goldring and M. B. Goldring, "Changes in the osteochondral unit during osteoarthritis: structure, function and cartilage–bone crosstalk," *Nature Reviews Rheumatology*, vol. 12, no. 11, pp. 632-644, 2016-11-01 2016, doi: 10.1038/nrrheum.2016.148.

[25] G. H. Lo *et al.*, "The ratio of medial to lateral tibial plateau bone mineral density and compartment-specific tibiofemoral osteoarthritis," *Osteoarthritis Cartilage*, vol. 14, no. 10, pp. 984-90, Oct 2006.

[26] M. Wada, Y. Maezawa, H. Baba, S. Shimada, S. Sasaki, and Y. Nose, "Relationships among bone mineral densities, static alignment and dynamic load in patients with medial compartment knee osteoarthritis," *Rheumatology (Oxford)*, vol. 40, no. 5, pp. 499-505, May 2001.

[27] O. R. Madsen, O. Schaadt, H. Bliddal, C. Egsmose, and J. Sylvest, "Bone mineral distribution of the proximal tibia in gonarthrosis assessed in vivo by photon absorption," *Osteoarthritis Cartilage*, vol. 2, no. 2, pp. 141-7, Jun 1994.

[28] E. A. Messent, R. J. Ward, C. J. Tonkin, and C. Buckland-Wright, "Tibial cancellous bone changes in patients with knee osteoarthritis. A short-term longitudinal study using Fractal Signature Analysis," *Osteoarthritis Cartilage*, vol. 13, no. 6, pp. 463-70, Jun 2005.

[29] S. Clarke *et al.*, "Dual-energy X-ray absorptiometry applied to the assessment of tibial subchondral bone mineral density in osteoarthritis of the knee," *Skeletal Radiol*, vol. 33, no. 10, pp. 588-95, Oct 2004.

[30] E. A. Messent, J. C. Buckland-Wright, and G. M. Blake, "Fractal analysis of trabecular bone in knee osteoarthritis (OA) is a more sensitive marker of disease status than bone mineral density (BMD)," *Calcif Tissue Int*, vol. 76, no. 6, pp. 419-25, Jun 2005.

[31] N. B. Watts, "Fundamentals and pitfalls of bone densitometry using dual-energy X-ray absorptiometry (DXA)," (in eng), *Osteoporos Int*, vol. 15, no. 11, pp. 847-54, Nov 2004, doi: 10.1007/s00198-004-1681-7.

[32] C. G. Peterfy *et al.*, "Whole-Organ Magnetic Resonance Imaging Score (WORMS) of the knee in osteoarthritis," (in eng), *Osteoarthritis Cartilage*, vol. 12, no. 3, pp. 177-90, Mar 2004, doi: 10.1016/j.joca.2003.11.003.

[33] F. Eckstein, D. Burstein, and T. M. Link, "Quantitative MRI of cartilage and bone: degenerative changes in osteoarthritis," (in eng), *NMR Biomed*, vol. 19, no. 7, pp. 822-54, Nov 2006, doi: 10.1002/nbm.1063.

[34] J. S. Bauer and T. M. Link, "Advances in osteoporosis imaging," *Eur J Radiol*, vol. 71, no. 3, pp. 440-9, Sep 2009.

[35] J. D. Johnston. "Imaging Osteoarthritis." https://www.orthogate.org/articles/hip-and-knee/imaging-osteoarthritis

[36] W. D. Burnett *et al.*, "Proximal tibial trabecular bone mineral density is related to pain in patients with osteoarthritis," (in eng), *Arthritis Res Ther,* vol. 19, no. 1, p. 200, 09 2017, doi: 10.1186/s13075-017-1415-9.

[37] P. Omoumi, H. Babel, B. M. Jolles, and J. Favre, "Quantitative regional and sub-regional analysis of femoral and tibial subchondral bone mineral density (sBMD) using computed tomography (CT): comparison of non-osteoarthritic (OA) and severe OA knees," (in eng), *Osteoarthritis Cartilage,* vol. 25, no. 11, pp. 1850-1857, 11 2017, doi: 10.1016/j.joca.2017.07.014.

[38] W. D. Burnett, S. A. Kontulainen, C. E. McLennan, D. J. Hunter, D. R. Wilson, and J. D. Johnston, "Regional depth-specific subchondral bone density measures in osteoarthritic and normal patellae: in vivo precision and preliminary comparisons," (in eng), *Osteoporos Int,* vol. 25, no. 3, pp. 1107-14, Mar 2014, doi: 10.1007/s00198-013-2568-2.

[39] J. D. Johnston, S. A. Kontulainen, B. A. Masri, and D. R. Wilson, "A comparison of conventional maximum intensity projection with a new depth-specific topographic mapping technique in the CT analysis of proximal tibial subchondral bone density," (in eng), *Skeletal Radiol,* vol. 39, no. 9, pp. 867-76, Sep 2010, doi: 10.1007/s00256-009-0835-2.

[40] Y. Harada, H. W. Wevers, and T. D. Cooke, "Distribution of bone strength in the proximal tibia," *J Arthroplasty,* vol. 3, no. 2, pp. 167-75, 1988.

[41] J. Favre, J. C. Erhart-Hledik, K. Blazek, B. Fasel, G. E. Gold, and T. P. Andriacchi, "Anatomically Standardized Maps Reveal Distinct Patterns of Cartilage Thickness With Increasing Severity of Medial Compartment Knee Osteoarthritis," (in eng), *J Orthop Res,* vol. 35, no. 11, pp. 2442-2451, 11 2017, doi: 10.1002/jor.23548.

[42] N. A. Segal *et al.*, "The Multicenter Osteoarthritis Study: opportunities for rehabilitation research," (in eng), *PM R,* vol. 5, no. 8, pp. 647-54, Aug 2013, doi: 10.1016/j.pmrj.2013.04.014.

[43] W. B. Edwards and K. L. Troy, "Simulating Distal Radius Fracture Strength Using Biomechanical Tests: A Modeling Study Examining the Influence of Boundary Conditions," *Journal of Biomechanical Engineering,* vol. 133, no. 11, 2011, doi: 10.1115/1.4005428.

[44] U. D. Monu, C. D. Jordan, B. L. Samuelson, B. A. Hargreaves, G. E. Gold, and E. J. Mcwalter, "Cluster analysis of quantitative MRI T 2 and T 1ρ relaxation times of cartilage identifies differences between healthy and ACL-injured individuals at 3T," *Osteoarthritis and Cartilage,* vol. 25, no. 4, pp. 513-520, 2017-04-01 2017, doi: 10.1016/j.joca.2016.09.015.

[45] J. Victor, "Rotational alignment of the distal femur: a literature review," (in eng), *Orthop Traumatol Surg Res,* vol. 95, no. 5, pp. 365-72, Sep 2009, doi: 10.1016/j.otsr.2009.04.011.

[46] D. A. Wright, M. Meguid, O. Lubovsky, and C. M. Whyne, "Subchondral bone density distribution in the human femoral head," (in eng), *Skeletal Radiol,* vol. 41, no. 6, pp. 677-83, Jun 2012, doi: 10.1007/s00256-011-1270-8.

[47] U. D. Monu, C. D. Jordan, B. L. Samuelson, B. A. Hargreaves, G. E. Gold, and E. J. McWalter, "Cluster analysis of quantitative MRI T," (in eng), *Osteoarthritis Cartilage,* vol. 25, no. 4, pp. 513-520, 04 2017, doi: 10.1016/j.joca.2016.09.015.

[48] A. D. Speirs, P. E. Beaulé, K. S. Rakhra, M. E. Schweitzer, and H. Frei, "Increased acetabular subchondral bone density is associated with cam-type femoroacetabular impingement," (in eng), *Osteoarthritis Cartilage,* vol. 21, no. 4, pp. 551-8, Apr 2013, doi: 10.1016/j.joca.2013.01.012.

[49] A. D. Speirs, P. E. Beaulé, K. S. Rakhra, M. E. Schweitzer, and H. Frei, "Bone density is higher in cam-type femoroacetabular impingement deformities compared to normal subchondral bone," (in eng), *Osteoarthritis Cartilage,* vol. 21, no. 8, pp. 1068-73, Aug 2013, doi: 10.1016/j.joca.2013.04.016.

[50] J. D. Johnston, S. A. Kontulainen, B. A. Masri, and D. R. Wilson, "Predicting subchondral bone stiffness using a depth-specific CT topographic mapping technique in normal and osteoarthritic proximal tibiae," (in eng), *Clin Biomech (Bristol, Avon),* vol. 26, no. 10, pp. 1012-8, Dec 2011, doi: 10.1016/j.clinbiomech.2011.06.009 S0268-0033(11)00165-3 [pii].

[51] H. Babel *et al.*, "A Registration Method for Three-Dimensional Analysis of Bone Mineral Density in the Proximal Tibia," (in eng), *J Biomech Eng,* vol. 143, no. 1, Sep 2020, doi: 10.1115/1.4048335.

[52] H. Babel, P. Omoumi, K. Cosendey, H. Cadas, B. M. Jolles, and J. Favre, "Three-Dimensional Quantification of Bone Mineral Density in the Distal Femur and Proximal Tibia Based on Computed Tomography: In Vitro Evaluation of an Extended Standardization Method," *Journal of Clinical Medicine,* vol 10, no. 1, Jan 2021.

[53] J. D. Johnston, C. E. Mclennan, D. J. Hunter, and D. R. Wilson, "In vivo precision of a depth-specific topographic mapping technique in the CT analysis of osteoarthritic and normal proximal tibial subchondral bone density," *Skeletal Radiology,* vol. 40, no. 8, pp. 1057-1064, 2011-08-01 2011, doi: 10.1007/s00256-010-1001-6.

[54] J.-P. Pelletier *et al.*, "Risk factors associated with the loss of cartilage volume on weight-bearing areas in knee osteoarthritis patients assessed by quantitative magnetic resonance imaging: a longitudinal study," *Arthritis Research & Therapy,* vol. 9, no. 4, p. R74, July 2007, doi: 10.1186/ar2272.

[55] D. Hunter *et al.*, "Evolution of semiquantitative whole joint assessment of knee OA: MOAKS (MRI Osteoarthritis Knee Score)," *Osteoarthritis Cartilage,* vol. 19, no. 8, pp. 990-1002, 2011.

[56] J. D. Johnston, B. A. Masri, and D. R. Wilson, "Computed tomography topographic mapping of subchondral density (CT-TOMASD) in osteoarthritic and normal knees: methodological development and preliminary findings," *Osteoarthritis and Cartilage,* vol. 17, no. 10, pp. 1319-1326, 2009-10-01 2009, doi: 10.1016/j.joca.2009.04.013.

[57] C. C. Glüer, G. Blake, Y. Lu, B. A. Blunt, M. Jergas, and H. K. Genant, "Accurate assessment of precision errors: how to measure the reproducibility of bone densitometry techniques," (in eng), *Osteoporos Int,* vol. 5, no. 4, pp. 262-70, 1995, doi: 10.1007/BF01774016.

[58] H. Yoav Benjamini and Yosef, "Controlling the False Discovery Rate: A Practical and Powerful Approach to Multiple Testing , urldate = 2022-09-23," *Journal of the Royal Statistical Society. Series B (Methodological),* vol. 57, no. 1, pp. 289-300, 1995.

[59] H. Babel *et al.*, "An Expert-Supervised Registration Method for Multiparameter Description of the Knee Joint Using Serial Imaging," *Journal of Clinical Medicine,* vol. 11, no. 3, p. 548, 2022-01-22 2022, doi: 10.3390/jcm11030548.

[60] P. A. a. B. M. J. a. J. F. Hugo Babel and Patrick Omoumi and Thomas, "New insight on the subchondral bone and cartilage functional unit: Bone mineral density and cartilage thickness are spatially correlated in non-osteoarthritic femoral condyles," *Osteoarthritis and Cartilage Open,* vol. 2, no. 3, p. 100079, 2020, doi: https://doi.org/10.1016/j.ocarto.2020.100079.

APPENDIX A
INITIAL ORIENTATION AND PRE-ALIGNMENT DETAILS

The first step of the pre-alignment stage is to use the k-means clustering algorithm to divide the distal femur object into two halves. This is done using the MATLAB k-means function with default parameters (MATLAB 2019) with the 3D coordinate locations of all voxels in the distal femur volume as inputs. After the distal femur object has been classified into two halves, the equation of the line joining both centroids is determined. This line will not perfectly align with any anatomical axis, and is highly sensitive to anatomical variation, however, it is useful to approximate original transverse plane alignment. This is required as even in the small dataset used for this work, distal femur volumes exhibited original orientations at 45° or more off from an expected 'neutral orientation'. Figure A-1 provides a sample occurrence where this process was used to improve initial transverse orientations.

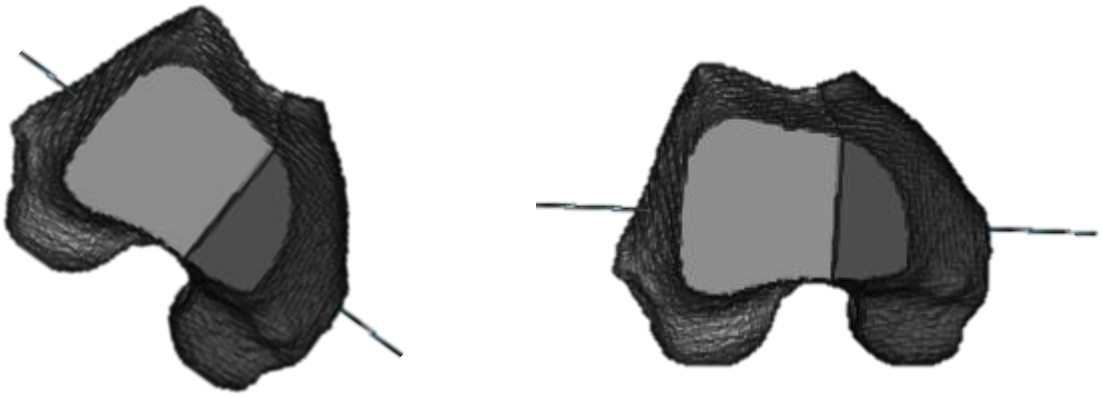

Figure A-1 Distal femur divided into k-means halves with centroid joining axis visible

A similar second issue which is addressed is the handling of distal femur volumes which are 'flipped' 180° in the transverse plane. This issue occurred for several images in the dataset used. To address this, the line joining the k-means centroids is used again. Volume is computed above and below the centroid line at a perpendicular angle near the line midpoint. Due to lack of bone between the condyles, the direction which exhibited lower volume is considered to be posterior and flipped if required. Figure A-2 shows a diagram illustrating this process.

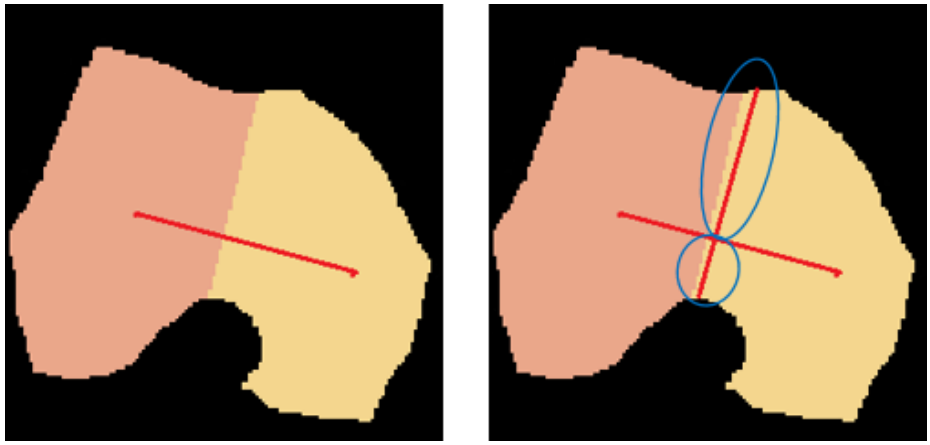

Figure A-2 Schematic showing geometric technique used to determine transverse plane orientation

Lastly, in order to standardize density measures for all participants, regardless of which knee was imaged, a left/right flipping protocol was implemented. This is done via searching for the transverse slice which first contains both halves of the k-means classified femur. Due to the lateral side of the distal femur being bulkier proximally, this end of the k-means volume will exhibit significantly more voxels belonging to the lateral half. By then comparing the k-means centroids, we can make an appropriate horizontal flip if required. Figure A-3 shows a sample transverse slice illustrating the disparity between medial and lateral halves when using the k-means algorithm. This concludes the 'pre alignment' step.

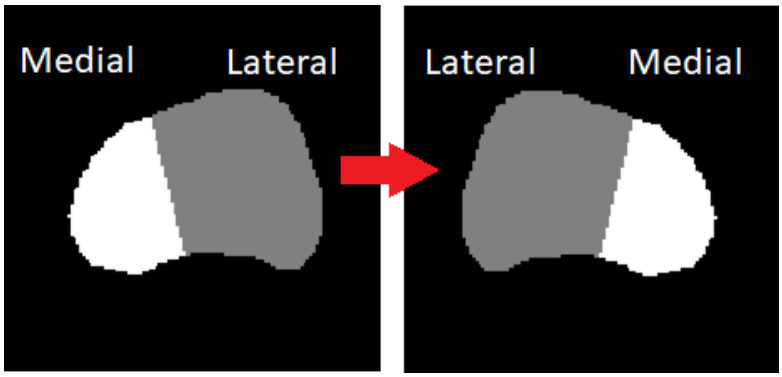

Figure A-3 Schematic showing geometric technique using the k-means algorithm used to differentiate between left and right distal femora

APPENDIX B
ALIGNMENT DETAILS

A critical step of the alignment workflow lies in the creation of the ‘shell’ image. It is created by simply subtracting two binary sagittal slices; the first is located roughly at the intercondylar fossa or ‘mid’ slice (where sagittal area is lowest), and the second is located at the center of a condyle (where sagittal area is highest). Figure B-1 illustrates this process.

Figure B-1 Schematic showing technique used to generate ‘shell’ image. Sagittal slices of: left - condyle center, middle – intercondylar fossa, right – resulting shell image

However, this process can fail depending on the geometry and initial alignment of the distal femur. Therefore, a function was created which ensures an acceptable shell image is created. An acceptable shell image must have two qualities: 1) Be a single connected component, 2) The height of the most proximal posterior and anterior ends of the image (ends of the horseshoe shape) be within 5 pixels of each other. If a shell image has posterior and anterior ends which are not similar heights, the mid slice is eroded (on the side which is shorter) until the two ends have similar heights. This process is also repeated until only a single connected component is present (Figure B-2). This approach was taken as it provides a method to consistently produce an acceptable shell image with the least amount of modification to the distal femoral shape.

Figure B-2 Sample diagram showing the iterative process to achieve suitable shell image by the thickening of the anterior portion

After an acceptable shell image is obtained, the thickness of the shell is computed for each angle with respect to the femoral centroid, resulting in a plot which characterizes its shape. The angles representing the edges of the femoral neck opening can be easily found at the edges of the span of zeros (Figure B-3). The femoral anatomical axis is then calculated as the average of the two angles (Figure B-4). A second plot is created by applying a median filter, computing the gradient and multiplying by -1 (Figure B-5).

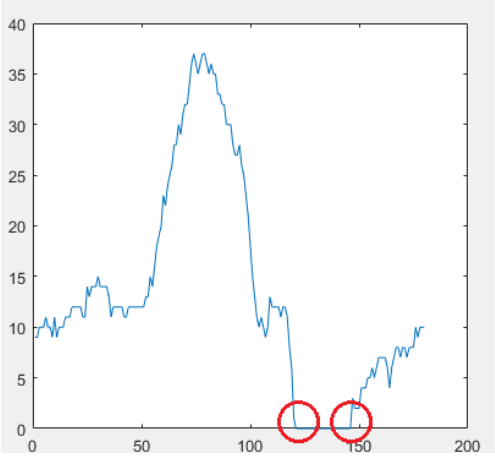

Figure B-3 Plot showing angle span of femoral neck with no pixels

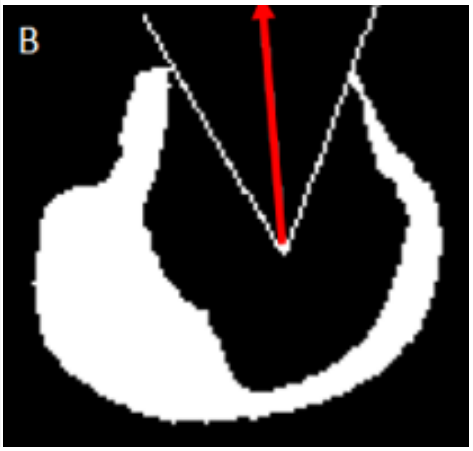

Figure B-4 Resulting femoral anatomical axis from averaged edges of femoral neck

This second plot will have peaks where there are significant drops in thickness. We then look for the largest drop (highest peak) that is not within 5 units (10° degrees) of the posterior opening point (as the transition to the femoral neck opening will also create a large drop). The built-in MATLAB findpeaks() function with default parameters was used for this end. This angle is treated as the transition point from the condyle to femoral neck and will be used for subchondral region placement. The anterior angle is found by reflecting this angle with the femoral

anatomical axis. Determining these angles are the final steps required before proceeding with subchondral surface delineation.

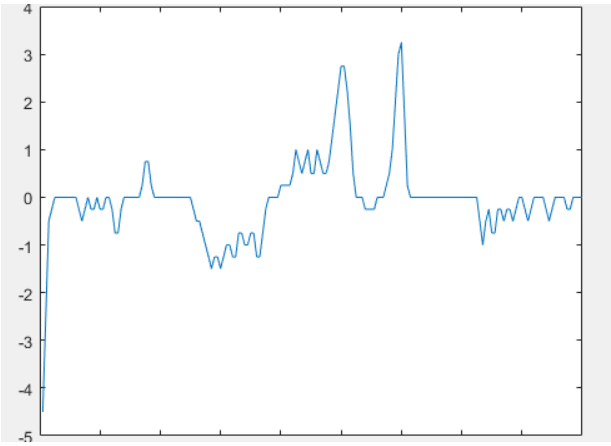

Figure B-5 Second plot showing peaks at locations with significant drops in thickness. The first peak being used for the approximate angle where the condyle transitions to the femoral neck. The second peak corresponds to the gap at the femoral neck and excluded during the peak detection process

APPENDIX C

SUBCHONDRAL SURFACE TEMPLATE-BASED DETAILS

The first step of the template-based subchondral surface definition process is to locate specific landmarks of the distal femur. These landmarks need only to demarcate between predefined sagittal regions which help to adjust the template to match the specific geometries of the current distal femur. 7 planes are defined; 4 planes define the lateral and medial edges of both condyles, 2 planes define approximate centers of both condyles, and 1 plane is used to mark the center of the intercondylar fossa. The 4 planes which define the edges of the condyles are found by first locating coronal slices which contain the condyles before they join at the main body of the femur. All volume anterior of this plane is removed, leaving a portion of the condyles (Figure C-1). The portion of the condyles present in this volume will exhibit widths very close to that of the full condyle, and its edges can be easily located via its bounding box. This is done because the condyles widen to form the epicondyle, though the subchondral surface does not follow this geometry. The other three planes are found by simply locating the sagittal slice with the least area (near the center) and the slices with the most area on either side of it. These landmarks are also predefined on the subchondral template so that it can be locally stretched and compressed to line up with those found on the distal femur volume. Figure C-2 shows these landmark planes for the 3D volume and cartilage template.

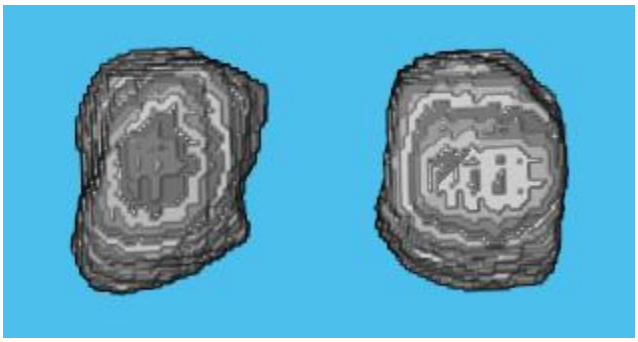

Figure C-1 Posterior ends of condyles, used for determining subchondral medial and lateral edges

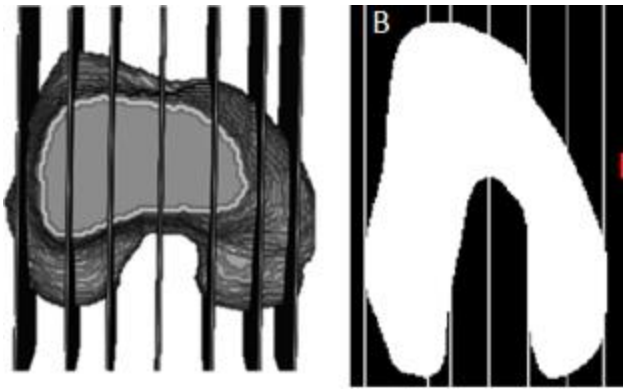

Figure C-2 Sagittal plane landmarks located and their corresponding locations on the cartilage template

The most anterior and posterior angles of the subchondral surface (process described in Appendix B) act as global max and min values for the template, with all values in between linearly interpolated. The process of applying the adjusted subchondral template to the distal femur is done one sagittal slice at a time. The span of angles which are present at the specific sagittal slice in the adjusted template are used to create local min/max values which define the span of subchondral voxels in that slice of the distal femur volume. Figure C-3 provides a diagram illustrating this angle scheme.

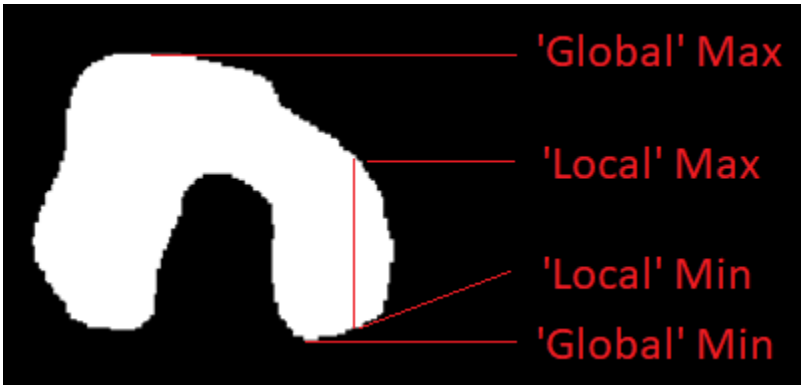

Figure C-3 Diagram showing angle scheme used to define the span of angles deemed to be subchondral current sagittal slice

To convert from the span of angles constituting the subchondral surface to the 3D volume, all voxels of the femur are assigned a value based on the angle they form with the centroid and are removed if they fall outside the current local min/max angles (repeated for each sagittal slice).

This process is outlined in figure C-4. This marks the final step of the template-based subchondral region definition.

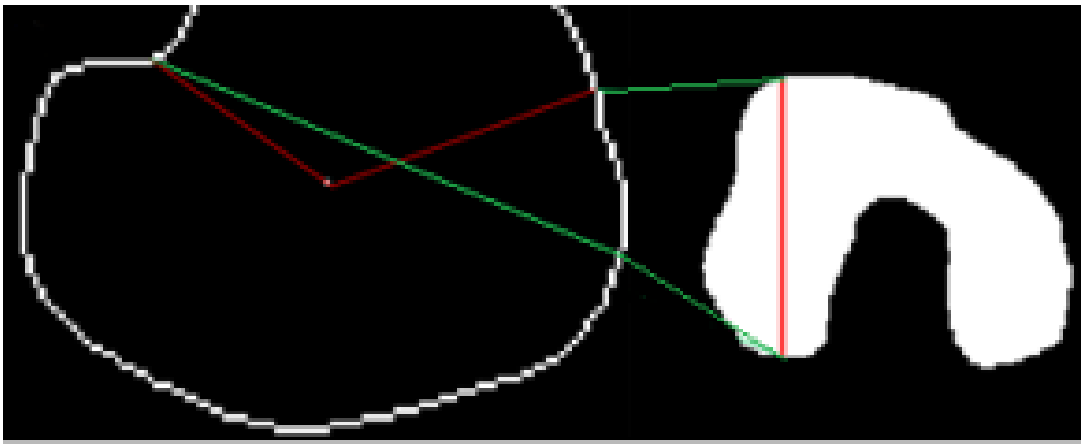

Figure C-4 Diagram showing a sample sagittal slice corresponding to a location on the cartilage template. The current minimum and maximum angles are computed based on their relative heights on the 2D cartilage map and correspondingly applied to the 3D volume (one sagittal slice at a time)

APPENDIX D
SUBCHONDRAL SURFACE REFINEMENT DETAILS

The subchondral surface refinement process begins with creating the 2D angular BMD/distance maps. A 'layered' femur object is created by erosion, whereby voxels which are removed by the nth erosion are assigned a value of n. This process is repeated 12 times (to get a maximum depth of 12 voxels or 7.5mm). A sagittal slice of this layered femur object is presented in Figure D-1.

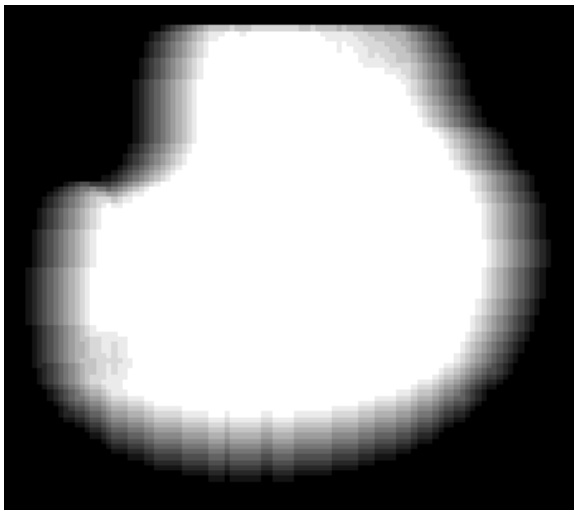

Figure D-1 Sample sagittal slice of the layered femur object

The 2D angular maps are created layer by layer (i.e., giving us stacks of 2D maps), with each layer corresponding to a specific depth. This is done by indexing the layered femur object for the current layer being created, and assessing the corresponding sagittal values, angle w.r.t. centroid, and BMD values at those indexed voxels. This results in 3 variables which can be entered into the MATLAB scatteredInterpolant() function with default parameters to create a 3 dimensional plot which describes the distribution of BMD as function of sagittal and angular positioning. By replacing the BMD variable with distance w.r.t. to the centroid, the 2D angular distance interpolant is similarly created. After the interpolant objects are created, we can create the 2D maps by querying the interpolants at regular intervals (starting and ending based on the estimated start and end of the subchondral surface). For this work, each pixel was set to represent 0.5°, though this variable only modulates how elongated the 2D maps appear and therefore was not adjusted or experimented with. Figures D-1 and D-2 provide a sample slice of both 2D maps.

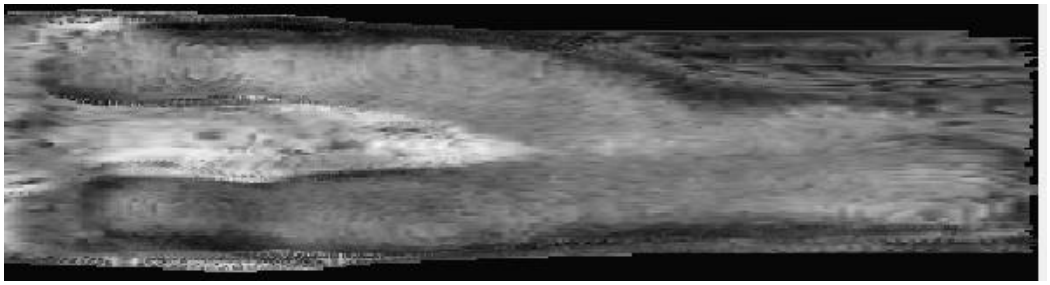

Figure D-2 Sample layer of 2D BMD map

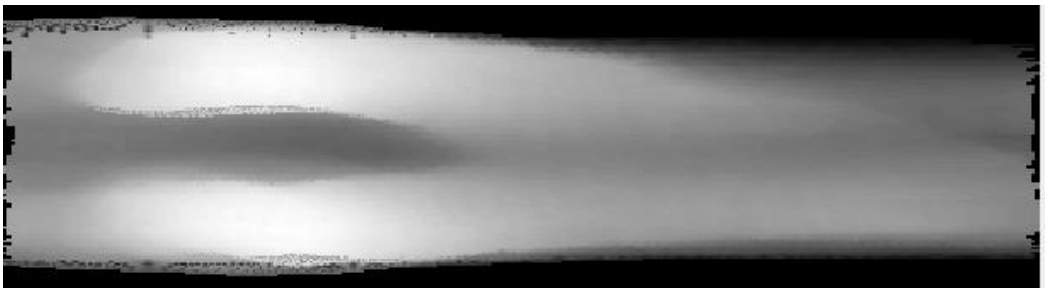

Figure D-3 Sample layer of 2D distance map

The 2D angular distance map is then used to refine the posterior end points of the subchondral map. Plots are generated which characterize the change in intensity as a function of angular position at the posterior end of each condyle. Using the previously estimated posterior end angles as a starting point, a nearby drop in intensity (indicating the transition from condyle to femoral neck) is found and used as the new posterior end angle. Next, a cropped image of the condyle end is fed into a region growing segmentation subroutine with the seed point corresponding to the brightest pixel in the cropped image. A range of acceptable pixel intensities (based on initial average intensities and the current iteration) are used to create an estimated segmentation. This segmentation is refined via the MATLAB imreconstruct() function with default parameters and additional smoothing operations. The range of acceptable pixel intensities are adjusted until the resulting segmented area reaches the posterior end angle previously found. This is done to improve the general shape of the subchondral surface at this area. Figure D-4 provides an example output of the segmented posterior end of a condyle. The most posterior point reaches the estimated max posterior angle for that condyle (shown as a black line).

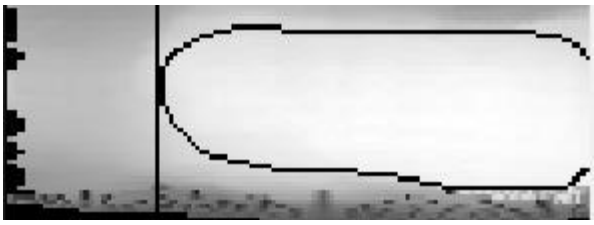

Figure D-4 Sample output of the region growing subroutine used iteratively until the posterior end of the condyle matches the estimated max posterior angle for that condyle

APPENDIX E
ROI DEFINITION AND METHODOLOGY DETAILS

This appendix will outline the methodology in which the ROIs used in this work were defined and applied to each distal femur volume. The Pelletier ROI was adapted slightly from the original cartilage map. The original anterior region had medial and lateral halves, though since the MOAKS ROI would replicate this, they were combined into a single region. Additionally, it was observed through BMD heat maps that regions of high density would typically occur centrally in the anterior region, therefore it was hypothesized that a single region may capture these density patterns more effectively.

To apply the 2D cartilage maps to the 3D volume, the point at which the condyles met was found in the 2D angular maps and converted into the appropriate angle in 3D space. It was then used along with the most posterior angle to create a span of angles. The posterior are created by dividing this span into thirds and differentiating between the medial and lateral halves. The anterior trochlear region is created from all remaining voxels. The Pelletier ROI diagram and 3D coloured volume is provided in Figure E-1.

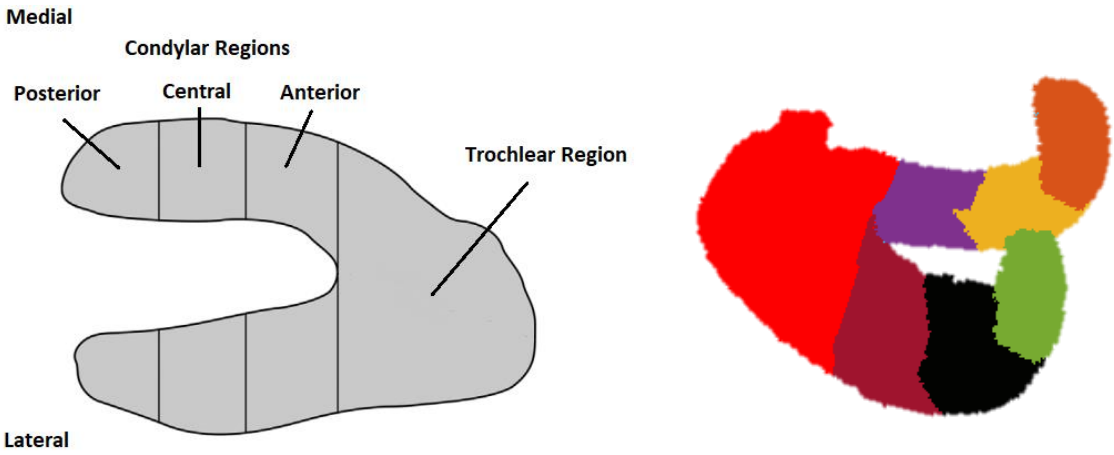

Figure E-1 Pelletier ROI Diagram and 3D Coloured Volume

The MOAKS ROI required some modifications from the original published methodology. First, the margins between regions are defined via the anterior and posterior aspects of the tibia in the original MOAKS sub regions. This was modified as access to tibial geometry and location would be required, information not available in the scope of this work. Instead, the angular span of the

subchondral surface was divided into equal thirds to provide a rough approximation of the original regions. Secondly, the physeal line demarked the superior border of the regions in the original MOAKS arrangement. This detail was not needed for this work, as the extreme ends of the subchondral surface acted as 'cut-offs' for the regions. The MOAKS ROI diagram and 3D coloured volume is provided in Figure E-2.

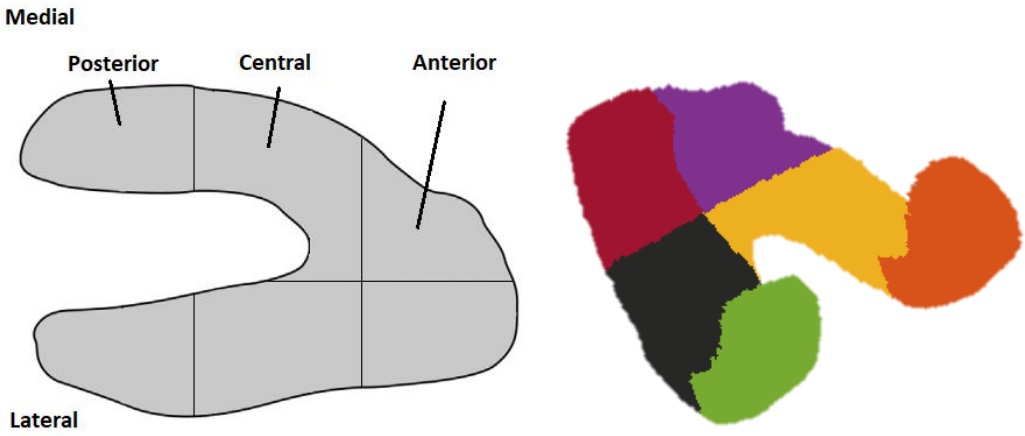

Figure E-2 MOAKS ROI Diagram and Coloured 3D Volume

Lastly, a small area in the medial-central region was removed for an additionally tested region as high-density voxels from the intercondylar fossa are situated here. This was done to test the effects of removing these voxels as they are not directly involved with joint contact and were hypothesized to be a source of error for density analyses at the distal femur. Figure E-3 provides a diagram showing which area was removed with a corresponding 3D coloured volume.

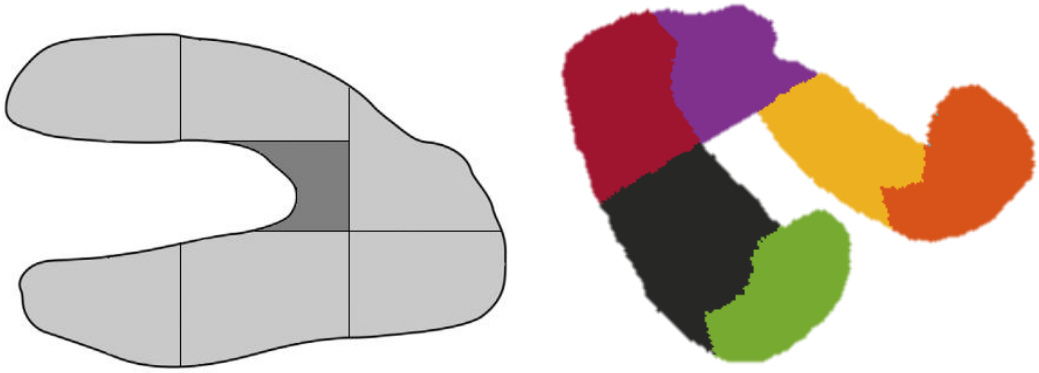

Figure E-2 Additional MOAKS Region Diagram and Coloured 3D Volume